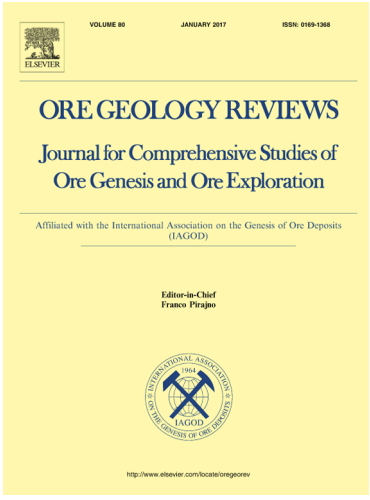

Trace element systematics and ore-forming processes in mafic VMS deposits: Evidence from the Troodos ophiolite, Cyprus

Andrew J. Martin, Manuel Keith, Iain McDonald, Karsten M. Haase, Katie A. McFall, Reiner Klemd, Christopher J. MacLeod

PII: S0169-1368(18)30805-9
DOI: https://doi.org/10.1016/j.oregeorev.2019.01.024
Reference: OREGEO 2810

To appear in: *Ore Geology Reviews*

Received Date: 18 September 2018
Revised Date: 7 January 2019
Accepted Date: 23 January 2019

Please cite this article as: A.J. Martin, M. Keith, I. McDonald, K.M. Haase, K.A. McFall, R. Klemd, C.J. MacLeod, Trace element systematics and ore-forming processes in mafic VMS deposits: Evidence from the Troodos ophiolite, Cyprus, *Ore Geology Reviews* (2019), doi: https://doi.org/10.1016/j.oregeorev.2019.01.024

Trace element systematics and ore-forming processes in mafic VMS deposits: Evidence from the Troodos ophiolite, Cyprus

Andrew J. Martin[(a*)], Manuel Keith[(b,c)], Iain McDonald[(a)], Karsten M. Haase[(d)], Katie A. McFall[(a)], Reiner Klemd[(d)] and Christopher J. MacLeod[(a)]

[a] School of Earth and Ocean Sciences, Cardiff University, Cardiff, CF10 3AT, UK

[b] School of Geography and Geology, University of Leicester, Leicester, LE1 7RH, UK

[c] Technische Universität Berlin, Institut für Angewandte Geowisseenschaften, 10587 Berlin, Germany

[d] GeoZentrum Nordbayern, Friedrich-Alexander-Universität Erlangen-Nürnberg, D-91054 Erlangen, Germany

[*]Corresponding author: Andrew J. Martin, e-mail: MartinAJ4@cardiff.ac.uk

Abstract

The volcanogenic massive sulfide (VMS) deposits in the Troodos ophiolite (Cyprus) are ancient analogues for modern day seafloor massive sulfide mineralisation formed in a subduction zone environment. In this study we present the first detailed in situ study of trace elements in sulfides from twenty VMS deposits hosted in the Troodos ophiolite to better understand factors that influence the distribution, enrichment and incorporation of trace elements in different sulfide minerals.

On a mineral scale, trace elements exhibit systematic variations between pyrite, chalcopyrite and sphalerite. Pyrite preferentially incorporates As, Sb, Au and Te, whilst chalcopyrite is enriched in Co and Se. Sphalerite is trace element poor with the exception of Ag and Cd. Selenium averages 278 ppm (n= 150) in chalcopyrite but only 42 ppm (n=1322) in pyrite. Bismuth and Te in pyrite show a weak positive correlation (R^2= 0.41) in some VMS deposits possibly linked with the occurrence of Bi-telluride inclusions. Trace element concentrations also vary between colloform and euhedral pyrite, with an enrichment of Au, As, Sb, Cu and Zn in colloform compared to euhedral pyrite.

Time resolved laser ablation profiles reveal that the trace element distribution on a mineral scale is not uniform and varies with crystallographic effects, fluctuating physicochemical fluid conditions such as temperature, pH, fS_2, fO_2 and ligand availability during sulfide precipitation. Incorporation mechanisms in sulfides differ between elements in pyrite, Ag, As, Se and Pb are hosted in solid solution or as nanoscale inclusions, whilst Au, Sb and Te may form micro-scale inclusions.

On a regional scale (20 km) the distribution of trace elements exhibits systematic variations between three major structural domains; namely the Solea, Mitsero and Larnaca grabens. The VMS deposits of the magmatic-tectonic Solea graben are enriched in Se, Co, Te, Au and Cu relative to Mitsero, which is a purely extensional feature. Therefore, we hypothesise that a variable magmatic volatile influx related to a) 'magma' volume, b) migration of the magmatic-hydrothermal crack front and associated

brine liberation or c) a variation in protolith metal concentration are responsible for regional scale variations in VMS geochemistry. This is suggested to be intrinsically linked to the spreading architecture of Troodos.

Key words: LA-ICP-MS, VMS, Troodos, sulfides, magmatic volatile influx, pyrite

1. Introduction

Volcanogenic Massive Sulfide (VMS) deposits are important resources of base and trace metals (Barrie and Hannington, 1999; Galley et al., 2007; Mercier-Langevin et al., 2011). With the discovery of >500 active vent sites in a range of tectonic settings we turn to fossil analogues to better understand 3D relationships, alteration and mineral chemistry that lead to the enrichment of trace metals. Fossil analogues allow us to better understand the depth relationship of mineralisation and trace element distribution, whilst active Seafloor Massive Sulfide (SMS) systems provide direct information on fluid chemistry and mineral precipitation temperatures. Consequently, the combination of modern and fossil analogues provides important information on the distribution of trace metals that may be key in the future feasibility and exploitation of SMS deposits (Boschen et al., 2013; Humphris et al., 1995; Humphris and Klein, 2018).

Volcanogenic Massive Sulfides form through the interaction of heated evolved seawater with newly formed oceanic crust and the subsequent precipitation of sulfides due to seawater mixing at or near the seafloor (Franklin et al., 2005; Galley et al., 2007; Hannington et al., 2011). Seawater penetrates into the crust and is progressively heated by thermal transfer from the underlying heat source with fluids reaching greenschist facies temperatures (350-400˚C) (Humphris and Klein, 2018; Jowitt et al., 2012). At these temperatures an pH ~2, widespread ion exchange occurs between wall rock and the hydrothermal fluid (e.g. Jowitt et al., 2012; Patten et al., 2017; Seewald and Seyfried Jr., 1990). This buoyant metal rich fluid ascends to the seafloor, upon exhalation it forms sulfide mineralisation that may be preserved as VMS ores (Galley et al., 2007; Hannington et al., 2011).

Subduction zone magmas commonly reach volatile saturation during differentiation in the crust, which results in the release of magmatic volatiles potentially rich in Cu, Au, Pb, As, Tl and other trace metals that can be contributed to the overlying hydrothermal system (de Ronde et al., 2011; Keith et al., 2018; Herzig et al., 1998; White and Hedenquist, 1990; Williams-Jones and Heinrich, 2005; Wohlgemuth-Ueberwasser et al., 2015). It is now widely accepted that the Troodos ophiolite hydrothermal systems and associated VMS deposits are fossil analogues to modern systems actively forming on the ocean floor (e.g. Franklin et al., 1981; Hannington et al., 1998; Humphris and Klein, 2018; Monecke et al., 2014).

Physicochemical fluid parameters such as temperature, pressure, fO_2, fS_2 and pH control metal and ligand (Cl^-, HS^-, H_2S and OH^-) solubility and transport in the hydrothermal system (Seewald and Seyfried, 1990; Seyfried and Bischoff, 1977). Furthermore, these are influenced by local parameters including host rock geochemistry, permeability, water-rock ratios, the potential contribution of magmatic volatiles and the water depth (Metz and Trefry, 2000; Mottl and Holland, 1978). Both, experimental studies (e.g. Seewald and Seyfried Jr., 1990; Seyfried and Bischoff, 1977) and fluid chemistry (e.g. Koschinsky et al., 2008; Metz and Trefry, 2000) provide evidence for the behaviour of metals in SMS systems. However, in fossil VMS systems pristine fluid information is not available. Instead mineralogy and mineral chemistry provide evidence of past physicochemical ore-forming conditions. Hence, the comparison of ancient VMS with active SMS systems allows us to constrain ore-forming processes in modern systems, their alteration and evolution over time.

Metal zonation in fossil VMS occurs due to zone refining, a process synonymous with mature SMS; low temperature Zn and Pb (<200˚C- Reed and Palandri, 2006) are mobilised and re-precipitated by subsequent fluid pulses. Copper occupies only the high temperature >265˚C central mound and stockwork (Herzig and Hannington, 1995). Pyrite is ubiquitous in VMS mineralisation, commonly occurring as low-temperature colloform and high temperature euhedral varieties (Keith et al., 2016b). Pyrite often contains appreciable concentrations of economic and/or deleterious trace elements, such as Au, As, Te, Se and Sb (Genna and Gaboury, 2015; Hannington et al., 1999; Keith et al., 2016a,b; Layton-Matthews et al., 2008).

Phase separation is directly related to temperature, pressure (i.e. formation depth) and salinity (Monecke et al., 2014; Schmidt et al., 2007). Evidence for supercritical fluids can be inferred from fluid inclusions in fossil VMS systems (e.g. Kelley and Robinson, 1990; Kelley et al., 1992). At 5˚S on the Mid Atlantic Ridge (MAR) fluids are intermittently vented at 464 ˚C (average 407 ˚C; 3000 m depth; Koschinsky et al., 2008), well above the critical point of seawater and thus sub-seafloor phase separation may be important in generating metal and chloride rich brines in SMS systems that may be important for metal enrichment in fossil analogues, if the brine is contributed to the overlying hydrothermal system (de Ronde et al., 2011; Keith et al., 2016b; Koschinsky et al., 2008). Kelley and Robinson (1990) and Kelley et al. (1992) pointed out the importance of metal-rich brines in the fossil Troodos hydrothermal systems.

Back-arc spreading centres and submerged island arc volcanoes account for 34 % of known vent sites (Hannington et al., 2005; Humphris and Klein, 2018). Seafloor sulfide mineralisation in these environments is typically enriched in Zn, Pb, Au, Ag, Te, Se, Sb, Tl, As and Bi compared to MOR hydrothermal systems, which are interpreted to be due to the contribution of a magmatic volatile

component derived from subduction zone-related magmas (Dekov et al, 2016; Herzig and Hannington, 1995; Humphris and Klein, 2018; Moss and Scott, 2001).

Fossil analogues of back-arc spreading environments represent ideal natural laboratories to investigate the distribution and incorporation mechanisms of different trace elements in hydrothermal sulfide ores and their host minerals. The Troodos ophiolite (Cyprus) formed in a subduction zone environment possibly associated with back-arc spreading, and therefore may exhibit an enrichment in magmatic volatile elements (Hannington et al., 1998; Regelous et al., 2014; Robertson and Xenophontos, 1993). Hence, the VMS systems hosted in the Troodos ophiolite offer the opportunity to study the processes of ore-formation and trace metal enrichment with respect to spatial and temporal changes in the tectonic regime of subduction zone-related rift structures.

2. Geological overview and sample localities

The Late Cretaceous (~92 Ma) Troodos ophiolite is located in the eastern Mediterranean (Figure 1) comprising a complete, almost undisturbed sequence of oceanic lithosphere hosting fossil hydrothermal systems; the type locality for Cyprus-type or mafic VMS deposits (Cox and Singer, 1986; Galley et al., 2007; Gass, 1980). Whilst the exact tectonic environment of formation remains debated, it is now widely accepted that Troodos formed in a supra-subduction zone environment (Miyashiro, 1973; Pearce et al., 1984; Pearce and Robinson, 2010; Regelous et al., 2014).

Three original seafloor rift structures are preserved on the northern flank of the Troodos ophiolite comprising the Larnaca, Mitsero and Solea grabens (Figure 1) (Varga and Moores, 1985). The graben axes are defined by inversely dipping sheeted dykes on either side of the axis (Moores and Vine, 1971; Varga and Moores, 1985; Varga et al., 1999). Grabens formed in periods of magmatic quiescence when spreading was accomplished through thinning of the upper crust via detachment faulting and rotation of upper crustal blocks in a 'bookshelf' manner (Nuriel et al., 2009; Varga and Moores, 1985). Associated with these prominent graben bounding faults are numerous VMS deposits (e.g. Adamides, 2010; Allerton and Vine, 1991; Constantinou, 1980- Figure 2).

Faulting related to graben formation was important in increasing the permeability of newly formed oceanic crust and facilitating large-scale hydrothermal fluid convection. Epidosites, which are zones of intensely altered sheeted dykes are widely documented at Troodos (e.g. Lemithou, Jowitt et al., 2012; Kelley et al., 1992; Richardson et al., 1987). They are interpreted as a source of metals for the overlying VMS systems (Jowitt et al., 2012; Patten et al., 2017). Volcanogenic massive sulfide ores occur in two main morphologies; shallow massive exhalative sulfide ores and sub-seafloor stockwork

ores (Hannington et al., 1998, 1990). Due to historic mining dating from pre-Roman times the mound mineralisation is not always preserved.

In total, samples from twenty different VMS deposits were investigated in this study. These have subsequently been classified into districts based on their corresponding structural domain (summarised in Table 1, Figure 2). For the purpose of this study we simplify the original classification by Moores et al. (1990) into five domains, from east to west: Larnaca, Southern Troodos Transform Fault Zone (STTFZ), Mitsero, Solea and Polis (Table 1, Figure 2). Structural domains are classified based on dip direction of the sheeted dyke complex (after Moores et al., 1990; Figure 2).

The wide geographical spread of samples and diverse range of ore types including massive, disseminated, semi-massive and jasper rich morphologies ensures that a wide range of ore-forming processes are investigated within and between different structural domains (Figure 1 and 2, Table 1). Hence, the data is representative for regional scale ore-forming processes related to spreading centre evolution.

3. Methods

Electron microprobe analysis (EMPA) was performed for selected sulfide samples to obtain major element data. Concentrations were obtained using a JEOL JXA-8200 Superprobe at the GeoZentrum Nordbayern. The quantitative EMP analyses were performed with a focused beam using an accelerating voltage of 20 kV and a beam current of 20 nA. The electron microprobe was calibrated by the following standards: FeS_2 (Fe,S), $CuFeS_2$ (Cu) and ZnS (Zn).

Laser Ablation ICP-MS (LA-ICP-MS) was used to determine in situ trace element concentrations in hydrothermal sulfides from 20 VMS across Troodos. Spot (n= 1558) and line (n =7) analyses were performed on polished blocks and thin sections (n=56) (Table 2). Elements analysed include ^{57}Fe, ^{65}Cu, ^{59}Co, ^{66}Zn, ^{75}As, ^{77}Se, ^{109}Ag, ^{111}Cd, ^{121}Sb, ^{125}Te, ^{185}Re, ^{189}Os, ^{193}Ir, ^{195}Pt, ^{197}Au ^{206}Pb and ^{209}Bi (see Appendix A1-A4). ^{77}Se was used preferentially over ^{82}Se due to lower interference levels from the Ar-Cl ablation gas. Analyses were carried out at the GeoZentrum Nordbayern (dataset A) and Cardiff University (dataset B, Appendix A1-A3).

Dataset A was analysed using a New Wave Research UP193 FX laser coupled to an Agilent 7500i ICP-MS. A single spot ablation pattern was utilised at a frequency of 15 Hz with a typical beam size of 25 µm, and on occasion 20 and 15 µm according to pyrite crystal size. Total acquisition time of each spot was 40 seconds including a 20 second gas blank prior to each analysis. Data set B was collected using a New Wave Research UP213 UV laser coupled to a Thermo X-series 2 ICP-MS. Samples were analysed in time resolved analysis mode at a frequency of 10 Hz and a nominal spot size of 55-80 µm depending

on the size of the analysed sulfide grain. Acquisition lasted 45 seconds with gas blank measured for 20 seconds prior to analysis.

Standards used for external calibration (dataset A) include Po724 B2 SRM (Au) (Memorial University Newfoundland) and MASS-1 (USGS) (V, Cr, Mn, Co, Ni, Cu, Zn, As, Se, Mo, Ag, Cd, Sb, Te, W, Pb, Bi). For dataset B calibration was performed using a series of synthetic NiFe-S standards and Memorial FeS (Memorial University Newfoundland) (S, Ni, Fe, and Cu as major elements and Co, Zn, As, Se, Ru, Rh, Pd, Ag, Cd, Sb, Te, Re, Os, Ir, Pt, Au, and Bi as trace elements- see Prichard et al., 2013).

Line analyses were performed at Cardiff University using a UP213 UV laser coupled to a Thermo X-series 2 ICP-MS. A 55 µm beam diameter was employed at a frequency of 10 Hz; ablation lasted between 80-120 seconds and a gas blank was measured for 20 seconds prior to analysis. The beam followed a pre-selected pattern designed to sample different sulfide phases. The sample translated at 6 µm/s relative to the laser.

Sulfur was used as an internal standard on all LA ICP-MS analyses. Sulfur measurements from EMP analyses (n =905) yielded average S concentrations for pyrite of 52.97 wt.% +/- 1.14 (2σ) (n=905), therefore the stoichiometric values of 53.4 to 53.5 wt. % for dataset A are within error of measured values for dataset B (see Appendix A1-A3). Similarly, S concentrations of 34.25 wt.% +/- 0.70 (2σ) in chalcopyrite are within error of the stoichiometric values for S (35-35.5 wt.%) used in dataset B.

4. Results

4.1 Ore petrography

Samples of sulfides have been classified into the following categories based on morphological and textural differences: massive (euhedral and colloform), semi-massive, stockwork, disseminated and jasper (Figure 3).

4.1.2 Pyrite

Pyrite is present in all samples analysed in this study (Table 1). The texture and morphology vary reflecting the fluid conditions under which it formed (e.g. temperature, fO_2, fS_2 etc.). Pyrite occurs as massive (>75%) (Figure 3 A and B), semi-massive (50-75%) (Figure 3 C), colloform (Figure 3 D and E), disseminated (10-20%) (Figure 3 F and G) and veined varieties (Figure 3 H). Within these textures, pyrite grains vary from euhedral to anhedral and rarely framboidal. Many pyrite grains exhibit a degree of dissolution; originally euhedral pyrite may be altered to subhedral or 'feathery' textures. Granular pyrite is common in the upper VMS stratigraphy with framboidal grains, associated with jarosite, goethite and covellite (Figure 3L). Resorbed grains commonly exhibit a porous or vuggy core; this is especially common for jasperitic samples where pyrite is intergrown with hematite and silica (Figure

3 E, I and L- yellow arrows). Inclusions of galena and sphalerite are present in some pyrite grains and are usually a few microns in size (via SEM).

4.1.3 Chalcopyrite

Chalcopyrite in massive pyrite samples (Figure 3 A, B, J and K and Table 1) forms interstitially as crude layers, surrounded by pyrite (Figure 3A and B). In stockwork samples massive chalcopyrite forms as aggregates of globular grains that are cut by secondary covellite-digenite (Figure 3 A, B, K). Disseminated chalcopyrite is rare and overprints early pyrite (Figure 3F). Secondary, seafloor or uplift-exposure related supergene alteration of chalcopyrite is evident in many VMS (e.g. Phoucasa or Apliki- Figure 3 K, L and M); in these samples chalcopyrite is variably altered to covellite and chalcocite.

4.1.4 Sphalerite

Sphalerite represents a minor constituent of the ores and was only observed at the Agrokipia B and the Mathiatis North VMS deposits (Table 1). It occurs as discrete subhedral crystals in veins and usually exhibits variable amounts of chalcopyrite disease (Figure 3 N and O). Sphalerite is commonly associated with pyrite and rarely with chalcopyrite (Figure 3 H, N and O).

4.2 Mineral Chemistry

The analysed sulfides show a distinct trace element distribution. Variations in trace element concentrations are observed between pyrite (n= 1322), chalcopyrite (n = 150) and sphalerite (n =86) (Figure 4, Table 2, 3 and 4). Pyrite contains elevated As, Te, and Sb relative to chalcopyrite and sphalerite. Chalcopyrite is notably enriched in Se over pyrite averaging 278 ppm (n= 150) in chalcopyrite but only 42 ppm (n=1322) in pyrite (Figure 4, Table 2 and 5). Sphalerite is depleted in most trace elements except Ag and Cd (Figure 4). Pyrite that co-precipitated with chalcopyrite is enriched in Cu with concentrations up to 1.1 wt.% (Table 2 Apliki, Figure 3M).

In pyrite, systematic variations between colloform and euhedral textures are observed, colloform pyrite is enriched in Ag, Cd and Mo relative to euhedral pyrite and depleted in Te, Co and Sb. Other elements exhibit no variation between different pyrite types. Gold at Skouriotissa, for example, has an average concentration of 0.5 ppm in both the euhedral (n=202) and colloform varaties (n=53). Most elements in pyrite (n=1322) display no notable correlation (linear R values- Table 3). Exceptions are Au and As that show a weak to moderate positive correlation (R^2= 0.46), as well as Pb and Ag (R^2= 0.31) and Cd and Zn (R^2= 0.53). On an ophiolite wide scale Te exhibits no corrleation with Bi in pyrite (R^2= 0.05). Pearson correlation coefficients (linear R values) between all elements analysed in pyrite are listed in Table 3, those for sphalerite and chalcopyrite can be found in Appendix A5.

4.3 Time Resolved Analysis

To resolve the distribution of trace elements in different sulfide phases, a series of time-resolved line analyses were carried out by LA-ICP-MS (Figure 5). Line analyses are essential to obtain information on trace element distribution and their incorporation mechanism down to a micron-scale. Additionally, time resolved analysis provided qualitative information on element concentration with count rate indicating the relative concentration of each given element. Three euhedral pyrites from Apliki (Figure 5E) exhibit variations in element concentrations between and within individual crystals, i.e. trace metal zonation. The variability in each element, i.e. a jagged (Figure 5 D- Te) or smooth appearance of the time resolved analysis profile (Figure 5 D- Se) may indicate their incorporation mechanism (see section 5.1).

5. Discussion

5.1 Mineral scale metal incorporation and distribution

Trace metal incorporation into sulfides is accomplished through either solid solution, i.e. lattice bound substitution, or as micro- to nanoscale mineral inclusions (Abraitis et al., 2004; Cook et al., 2009; Deditius and Reich 2016; Deditius et al., 2011; Genna and Gaboury, 2015; Gregory et al., 2015; Reich et al., 2013; Tardani et al., 2017; Wohlgemuth-Ueberwasser et al., 2015). The incorporation of trace elements depends upon physical and chemical fluid factors (e.g. temperature, fO_2, fS_2: Huston et al., 1995; Wohlgmuth-Ueberwasser et al., 2015, Revan et al., 2014; Keith et al., 2016a, b), as well as crystallographic effects including the valance states and covalent radii of different lattice bound elements (Reich et al., 2005; Keith et al., 2018).

We do acknowledge that LA-ICP-MS cannot distinguish between nanoscale inclusions and lattice bound elements, as these would both produce a smooth ablation profile (Gregory et al., 2015; Wohlgemuth-Ueberwasser et al., 2015). However, elements that display a jagged saw-tooth pattern most likely occur as mineral inclusions (Figure 5 B and D, Te).

Variation of elements in time resolved laser ablation profiles can be explained by different incorporation mechanisms of metals in pyrite. Huston et al. (1995) identified three groups of trace elements based on their incorporation mechanisms in VMS pyrite. This includes (1) Cu, Zn, Pb, Ba, Bi, Ag and Sb as micro- or nanoscale inclusions, (2) As, Tl, Au and Mo due to non-stoichiometric substitution and (3) elements with a stoichiometric substitution for S (Se and Te) and Fe (Co and Ni) (Chouinard et al., 2005; Huston et. al, 1995).

The incorporation mechanism of Te remains debated with Huston et al., (1995) and Butler and Nesbitt (1999) favouring its incorporation in solid solution. Given the larger covalent radii of Te (1.38 Å; Cordero et al., 2008), substitution in solid solution in pyrite is unlikely and Keith et al. (2018) prefer its

incorporation as micro- to nanoscale inclusions. Analysis from this study for Te do not favour one single incorporation mechanism; instead Te incorporation appears variable and depends on the sample analysed. Tellurium in pyrite from Apliki exhibits a saw tooth ablation profile (Figure 5 D and E) suggesting incorporation of Te as microscale inclusions compared with Se that has a smooth ablation profile suggesting that Se occurs in solid solution substituting S in pyrite and chalcopyrite (Huston et al., 1995; Maslennikov et al., 2009, 2017; Keith et al., 2018).

In contrast, pyrite from Skouriotissa exhibits a smoother profile for Te (Figure 5G) indicating nanoscale inclusions or a lattice bound appearance (Deditius et al., 2011). However, variations between pyrite grains suggest different incorporation mechanisms for Te that include nanoscale inclusions or solid solution at Skouriotissa (Figure 5 G) to microscale inclusions at Apliki (Figure 5 D and E).

It has been shown that As rich pyrite can incorporate high concentrations of trace elements compared to As poor pyrite either in solid solution or as inclusions (Reich et al., 2005; Deditius et al., 2014, 2011, 2008; Keith et al., 2018). Arsenic occurs in several oxidation states (-I, +II, +III, +V) and therefore may be substituted into the pyrite lattice either as an anion or cation depending on the prevailing redox conditions in the ore-forming fluid (Chouinard et al., 2005; Qian et al., 2013; Reich et al., 2005). Previous studies have identified $As(OH)_3$ as the major As species in reduced ore fluids (e.g. Pokrovski et al., 2002). Arsenic as an anion is incorporated in pyrite as a substitution with S and as a cation via a coupled substitution with Fe (Chouinard et al., 2005; Deditius et al., 2008). We assume that under reduced conditions As occurs as an anion in Troodos pyrite (e.g. Nesbitt et al., 1995; Simon et al., 1999). This suggests that As rich pyrite from the Troodos VMS deposits may contain appreciable trace elements concentrations.

Arsenic is used as a discrimination tool to decipher the incorporation of trace elements in the pyrite structrue i.e. their incorporation as a lattice bound substitution or as micro- or nano-particle inclusions (Figure 6- after Deditius et al., 2014; Keith et al., 2018; Reich et al., 2010, 2013). Data points for the elements considered (Au, Ag, Sb, Pb and Te) plot within the wedge-shaped zone (Figrue 6) which defines the upper solubility limits between mineral inclusions and lattice substituted elements. Concentrations which plot outside the wedge-shaped or toward the upper solubility limits of the zone suggest inclusions (red dashed line- Figure 6), while compositions in the wedge-shaped zone represent lattice bound substitutions or nanoscale-inclusions. When plotted in log-log space the solubility limits of Te and As in pyrite define a wedge shaped zone (after Keith et al., 2018). This indicates the solubility limits of Te in a lattice bound substitution and as inclusions (Figure 6 E). When applied to Troodos VMS pyrite, several points plot outside the wedge shaped zone and thus represent the occurrence of inclusions. We apply the Au solubility line (Figure 6A after Reich et al., 2005) defining the solubility

limits of Au^0 hosted as sub-micron inclusions to Te-As space (Figure 6E; black dashed line). Keith et al., (2018) suggest that a positive correlation between Au and Te (R^2=0.55) at low As but high Te-(Au) that Au telluride inclusions (e.g. calavarite $AuTe_2$) host appreciable Te. In Troodos VMS we find no correlation (R^2 = <0.01) between Au and Te. This strongly suggests the incorporation of Te in solid solution and less commonly mineral inclusions (Figure 5 E). Points that plot to the far right of the wedge-shaped zone (i.e. high As, low Te) could represent As rich mineral inclusions (e.g. Tennantite).

In this study we find that trace element incorporation into pyrite in the ancient Troodos VMS systems is almost identical to the modern analogues considered by Keith et al. (2016b; Figure 6). Most data for As-Au, As-Ag, As-Sb, As-Pb plot within the wedge-shaped zone and below the solubility limit (for Au). We find that a higher proportion of Sb and Pb points for Troodos plot outside the wedge-shaped zone at 7 and 25 % respectively compared to modern analogues at 3 and 6 % for Sb and Pb (Keith et al., 2016b). This relates in particular to Mathiatis North (Figure 6 C), where Sb reaches 2873 ppm at a maximum As content of 76 ppm. Additionally, we find that a higher proportion of Pb is inclusion-hosted in pyrite from the Troodos ophiolite, this is confirmed microscopically as galena inclusions in pyrite.

Telluride minerals were not observed in this study; however, previous studies highlighted the localised occurrence of tellurobismuthite (Bi_2Te_3) at Skouriotissa (Figure 7-Taylor, 2015). The systematic variation of Bi and Te in time resolved ablation profiles suggests that concentrations of Bi and Te exhibit a coupled relationship (e.g. Figure 5 A). However, Bi and Te exhibit no correlation (R^2=0.05) in pyrite across all VMS deposits. The Te-Bi correlation coefficients in pyrite vary between different deposits (Figure 7). This suggests variable incorporation mechanisms for Te, most likely in response to changes in the local physicochemical fluid conditions (e.g. temperature, fS_2, fO_2) and the concentrations of other lattice modifying trace elements, such as As (Figure 6; Keith et al., 2018). The best correlation between Bi and Te was observed in pyrite from the Apliki (R^2=0.35) and Phoucasa (R^2=0.32; Figure 7). In contrast, Se exhibits a smooth ablation profile that closely follows that of S (Figure 5 A and D) probably indicating a lattice bound substitution of Se for S (Huston et al., 1995).

Trace elements in chalcopyrite are hosted as two distinct groups identified by their incorporation mechanism; those incorporated as inclusions (e.g. Pb, Bi, Ba, Zn), or elements in a lattice bound substitution (e.g. Ag, In, Sn, Se, Zn) (Huston et al., 1995). Lattice bound substitution is achieved via either a simple substitution (e.g. $Zn^{2+} \leftrightarrow Fe^{2+}$ or $S^{2-} \leftrightarrow Se^{2-}$) or a coupled substitution (e.g. $2\ Zn^{2+} \leftrightarrow Cu^{+} + In^{3+}$) (Ye et al., 2011). The reader is directed to numerous references that address the incorporation of trace elements in chalcopyrite in further detail (e.g. Huston et al., 1995; George et al., 2018; Reich et al., 2013; Revan et al., 2014; Wohlgameth-Uberwasser et al., 2015).

Selenium concentrations are elevated in chalcopyrite compared to pyrite (Table 4 and 2). Selenium exhibits an order of magnitude variation within and between different VMS. At Apliki Se in chalcopyrite ranges from 103.7 to 3956 ppm; the higher concentrations are comparable to those reported by Butler and Nesbitt (1999) for the active Broken Spur vent field. The smooth time resolved profile (Figure 5C- Apliki) suggests that Se is hosted in a lattice bound substitution with S in chalcopyrite (Huston et al., 1995; Butler and Nesbitt, 1999). We suggest variation in Se concentration is due to local physicochemical factors relating to fluid temperature, magmatic influx or co-precipitating sulfide phases (Layton-Matthews et al., 2008; Huston et al., 1995). Increased magmatic influx favours high Se (e.g. de Ronde et al., 2005; Rouxel et al., 2004) whereas the precipitation of galena (or clausthalite - PbSe) would preferentially incorporate Se leading to a depletion in any co-precipitated chalcopyrite (George et al., 2018). Furthermore, Beteheke and Barton (1971) state that at 390 °C, chalcopyrite can incorporate up to 2150 ppm Se forming a solid solution with eskebornite ($CuFeSe_2$). Similar concentrations are observed in this study in chalcopyrite.

Tellurium concentrations in chalcopyrite are significantly less variable than in pyrite averaging 6.1 ppm (median 2.2 ppm). From 150 analysis (Table 4) 104 are above detection limit (~0.6 ppm). Several values at Phoucasa (44.1 and 171 ppm Te) are significantly higher than the average and median values. Elevated Te correlates with Au (4.30 and 3.58 ppm respectively) and Pt, Ir and Os signifying a possible Au-Pt-Te inclusion (Appendix 2B). This is consistent with observations from the Urals VMS where elevated Au and Te are attributed to telluride inclusions (e.g. calavrite - $AuTe_2$) (Maslennikov et al., 2009).

Zinc in chalcopyrite may be incorporated as both a solid solution element and as inclusions (Huston et al., 1995). Zinc concentrations <2000 ppm are suggested to be incorporated as a solid solution, possibly substituting for Fe and those >2000 ppm occur as inclusions (Huston et al., 1995). In Troodos, VMS Zn concentrations vary from below detection limit to 22.5 wt.% (Table 4); the latter clearly indicating sphalerite inclusions. For most VMS deposits the available data suggest the incorporation of Zn in a solid solution with median values of 292 ppm, well below the suggested 2000 ppm threshold.

Arsenic values are commonly below detection limit (22 detected out of 150; average ~1.5 ppm) with a maximum of 387.4 ppm at Kokkinoyia. These low but variable concentrations demonstrate the limited incorporation potential of As in chalcopyrite. At concentrations <2000 ppm, As is likely to be incorporated as a solid solution in chalcopyrite (Huston et al., 1995). This is supported by a smooth laser ablation profile for As in chalcopyrite in Troodos VMS (Figure 5E). Additionally, the As profile follows that of other elements hosted in solid solution (e.g. Se – Figure 5E).

Gold and Ag concentrations in chalcopyrite from Troodos VMS are low with 31 and 49 (of 150) analysis above detection limit for Au and Ag respectively (Appendix A2). Gold concentrations reach a maximum of 4.3 ppm and in some instances these high Au values correlate with increased Te and Pt suggesting at high concentrations Au is hosted as discrete mineral phases (e.g. Maslennikov et al., 2009). Gold is generally below 1 ppm in Troodos VMS (Table 4), comparable to concentrations in other VMS (Cook et al., 2011; Maslennikov et al., 2009; Revan et al., 2014).

Silver demonstrates similar variability in chalcopyrite to Au with a maximum value of 16.3 ppm (Three Hills). These low concentrations suggest that Ag is incorporated as Ag^+ as a lattice bound substitution with Cu^+ (Huston et al., 1995). Substantially higher Ag values in chalcopyrite are suggested to indicate the presence of argentiferous galena inclusions and in some instances elevated Pb correlates with increased Ag (Huston et al., 1995), however this was not directly observed in Troodos VMS. Concentrations of Ag between different VMS deposits are pronounced; at Apliki with one exception all analysis are below detection limit, whereas at Three Hills 12 of 15 analysis are above detection limit. We attribute this variation to the mineral scale partitioning of Ag between different sulfide phases, i.e. galena preferentially incorporates Ag (George et al., 2016, 2018; Large et al., 2009).

Bismuth, Cd and Sb may also form trace constituents in chalcopyrite (Table 4). Bismuth occurs consistently in minor amounts < 1 ppm throughout most chalcopyrite grains analysed; 82 analyses of 150 yield values above detection limit (>0.05 ppm). High Bi values are reported for Urals VMS and active SMS and are associated with inclusions of bismuthinite (Bi_2S_3) or bismuth tellurides (e.g. tellurobismuthite, Bi_2Te_3) (Gena et al., 2013; Maslennikov et al., 2012), however comparatively high values were not observed in Troodos. Cadmium concentrations in pyrite vary spatially between different VMS. This reflects variable amounts of co-precipitated sphalerite and its preferential incorporation of Cd over chalcopyrite. High Cd levels correlate with elevated Zn that probably indicate the analysis of Cd rich sphalerite inclusions (Table 4 and 5) (e.g. Cook et al., 2009; George et al., 2018). Cadmium concentrations range from below detection to 13.4 ppm (average: 0.81 ppm, median: 0.59 ppm). These observations are consistent with data from Huston et al. (1995) who state that Cd may occur as a lattice bound substitution in chalcopyrite at levels (<2000 ppm), however mineral inclusions and sulfosalts cannot be ruled out. Very little data is available on Sb incorporation and only 22 analysis of 150 in chalcopyrite returned concentrations above detection limit (Table 4). Huston et al. (1995) suggest that concentrations of Sb >500 ppm are hosted as mineral inclusions of tennantite-tetrahedrite series minerals. In Troodos VMS an R^2 value of >0.01 between As and Sb suggesting tennantite-tetrahedrite inclusions do not host significant Sb.

Sphalerite is poor host for trace elements in Troodos VMS compared with chalcopyrite and pyrite. The only element notably enriched in sphalerite is Cd with maximum concentrations of 3400 ppm at Kynousa (Table 5). Two groups of elements are identified in sphalerite; those forming inclusions (e.g. Ba and Pb) or elements hosted in a lattice bound substitution (e.g. Cd, Cu, Te, Ag) (Huston et al., 1995; Cook et al., 2009). Cadmium in Troodos VMS was above detection in all bar one analyses (n=85) and concentrations exhibit an order of magnitude variation between different deposits (Table 5). The smooth ablation profile for Cd in sphalerite (Figure 5F) that closely mimics Zn in shape suggests Cd is hosted as a lattice bound substitution element. Cook et al. (2009) state that Cd occurs in concentrations typically >0.2 wt% in sphalerite due to the substitution of Cd^{2+} with Zn^{2+}; this is likely the case in Troodos VMS.

Copper in sphalerite was detectable in most sphalerite grains analysed at concentrations between 0.09 to 8.97 wt.%. Huston et al. (1995) suggest that Cu values <1.6 wt.% are likely incorporated in a solid solution and erratically high values (>1.6 wt.%) probably result from chalcopyrite inclusions. This suggests that the majority of Cu in sphalerite at Skouriotissa is hosted as inclusions, and in some case visible chalcopyrite disease was present to confirm this. This is further supported by the time resolved analysis of sphalerite from Agrokipia (Figure 5F) where Cu at low concentrations >0.62 wt.% has a smooth ablation profile supporting its incorporation as a solid solution. All other elements (Ag, As, Sb, Pb and Se) occur in minor amounts <200 ppm (Table 5). Mathiatis North exhibits an enrichment in Se and Ag in sphalerite compared to all other deposits; with limited analyses available, the reason for this enrichment is unclear.

5.2 Physiochemical conditions of ore-formation

Colloform and euhedral pyrite show variable time resolved LA-ICP-MS profiles indicating that pyrite texture influences trace element concentrations (Figure 5 A and B). Aggregates of interlocking pyrite (Figure 5 A) form crude bands at the base of porous colloform pyrite (Figure 5 B). Microscopically multiple pyrite crystals can be distinguished (Figure 5A); laser ablation profiles across three pyrite grains indicate radial zonation in trace elements across different pyrite crystals (Figure 5 A). This demonstrates that the physicochemical conditions (e.g. temperature) of the fluid fluctuated temporally during pyrite precipitation. By comparison, Mo is also enriched in colloform pyrite relative to euhedral varieties; this is due to a seawater source of Mo (Kristall et al., 2011; Metz and Trefry, 2000; Keith et al., 2016a,b). A similar trend of trace element enrichment is reported in pyrite from Skouriotissa where deep euhedral pyrite is enriched in Te, Se and Co relative to colloform varieties (Keith et al, 2016b).

Sulfide mound growth is accomplished through the collapse and re-precipitation of sulfides that lead to zone refining in response to changes in fluid composition and the collapse and reworking of unstable chimney structures (Hannington et al., 1998; Herzig and Hannington, 1995; Revan et al., 2014). Oxygen fugacity, fS_2, temperature and pH vary spatially and temporally during mound growth and system maturation (e.g., Galley et al., 2007). Such variability is demonstrated by the laser ablation profiles showing variable trace element intensities from core to rim in euhedral pyrite reflecting changes in physiochemical fluid conditions and metal flux in the VMS systems (Figure 5 D and E). Whilst the exact nature of these changes cannot be distinguished, typically reduced conductive cooling, compaction of the sulfide mound and reduced seawater infiltration during maturation increases the precipitation temperatures, whilst fault movement facilitates seawater ingress and cooling leading to fluctuating fluid chemistry that in turn influences trace element incorporation leading to metal zonation in precipitating pyrite (Gillis and Roberts, 1999; Humphris and Cann, 2000; von Damm, 1990).

Four different types of pyrite mineralisation can be distinguished in the Troodos VMS ores; massive (Figure 3 B and K), colloform (Figure 3 D), stockwork (Figure 3 M) and jasper (Figure 3 I). These different pyrite types form in different regions of the VMS stratigraphy. Jasper (hematite + pyrite + silica) forms at the oxidised margins of the mound as centimetre scale veins, whilst euhedral pyrite forms in the high temperatures regions (Hannington et al., 1998). Colloform pyrite crystallised rapidly indicating disequilibrium conditions associated with the upper mound where seawater interaction is high and the temperatures are low (Berkenbosch et al., 2012; Keith et al., 2016a,b). No clear systematic variation in the trace element distribution in pyrite is noted with depth in the Skouriotissa ore body (i.e. shallow vs. deep stockwork) and we are unable to convincingly reproduce such systematic variations in other trace elements as reported by Keith et al. (2016a) for Te and Se. This strongly suggests that the trace element composition is influenced by complex physicochemical changes on the local scale (cm to m) along fluid pathways that govern trace element incorporation. Thus, explaining the poor systematic variation between trace elements in pyrite from Troodos VMS deposits (Table 3).

All jasper samples contain pyrite as the only sulfide phase. Chalcopyrite is absent, indicating that jasper precipitated at relatively low temperatures (<265˚C; Safina et al., 2016), and due to the inclusion of hematite, under relatively oxidised conditions. Trace element analyses show that pyrite associated with jasper is enriched in Se compared to other samples at Phoucasa averaging 193 ppm Se (n=17, σ= 132). Huston et al. (1995) and Keith et al., (2018) suggested that Se incorporation in pyrite favours lower temperatures and more oxidised conditions, however Hannington et al. (1998) and Auclair et

al. (1987) prefer Se enrichment at high fluid temperatures. In this study we support the observation that Se in pyrite is preferentially enriched in low temperature environments.

Chalcopyrite contains higher average Se (278 ppm, n= 150) compared to pyrite (42 ppm, n=1322). Therefore, we suggest that chalcopyrite-rich VMS ores (i.e. stockwork) at depth may cause a corresponding Se depletion in pyrite-rich ores, especially in the upper mound regions of the VMS deposit. Selenium in the hydrothermal fluids preferentially partitions into chalcopyrite in the deeper stratigraphic sections of VMS deposits and is therefore depleted in the hydrothermal fluids and associated sulfides at or near the seafloor (Rouxel et al., 2004). At temperatures <260˚C associated with the waning stages of the hydrothermal system, chalcopyrite precipitation ceases in response to cooling of the hydrothermal system. At these lower temperatures Se is no longer incorporated into precipitating chalcopyrite but instead migrates through the stockwork to the upper VMS stratigraphy where it is incorporated in pyrite and galena (if present- e.g. George et al., 2018). In this study on a regional scale we find extremely variable Se concentrations in pyrite and chalcopyrite range from <10 ppm to 4942 ppm and 7.5 to 3955 in pyrite (n=1322) and chalcopyrite (n=150) respectively. This variation can be explained by (1) co-precipitation of different sulfide phases and the preferential uptake of Se by chalcopyrite, and (2) the effect of zone refining and Se re-mobilisation into late stage pyrite (Martin et al., 2018).

Time resolved LA-ICP-MS analyses across multiple pyrite generations reveal concentric zoning of elements recording the evolution of the hydrothermal fluid and preferential incorporation of trace elements under temporally distinct physicochemical conditions. With no mineralogical (recrystallization or subsequent normal grain growth) or structural evidence of metamorphism (Gass, 1980), we assume that the trace element profiles preserved in pyrite from Troodos represent primary features, and thus have not been affected by later metamorphism leading to element mobilisation (Genna and Gaboury, 2015).

Time resolved spectra across three euhedral pyrite grains (Figure 5 E) show that euhedral pyrite 1 is depleted in Se, Te and Bi but enriched in Sb and Zn relative to euhedral pyrites 2 and 3. All pyrite grains contain elevated As but appear to be concentrically zoned with increased As counts measured in the centre of the grain. We suggest that these zones reflect temporal variations in physicochemical fluid conditions (e.g. pH, temperature) of the ore-forming fluid which are related to pulsed magmatic influx into the VMS system. If As concentrations in the fluid decrease leading to the precipitation of As poor zones, the ability of pyrite to incorporate Te as a solid solution or nanoscale-inclusions would decrease, hence at low As concentrations (<100 ppm) we see Te plotting outside the wedge shaped zone forming mineral-scale inclusions (cf. section 5.1; Figure 6 E).

In addition to changes in the local physicochemical fluid conditions, systematic variations in magmatophile trace elements in pyrite (Table 6: Se, Co, Cu, Te, Bi, Au- de Ronde et al., 2011) on a district or graben scale (~20 km) suggest a variable metal source, namely the host rocks or the potential contribution of magmatic volatiles to the hydrothermal system.

5.3 Source rock variation and trace element composition

Trace element variations on a district scale may be a function of (1) source rock composition or (2) a variable magmatic volatile influx; all of which ultimately relate to a magmatic source (Herzig et al., 1998; Jowitt et al., 2012; Patten et al., 2017; Yang and Scott, 2002; Keith et al., 2016a,b; 2018; cf. Lüders et al., 2002). The Troodos lithosphere formed in a subduction zone environment and lava geochemistry is significantly different from typical MORB, lavas are enriched in volatile elements, have a higher H_2O content and may be more evolved in composition (andesites, boninites etc.) (e.g. Kelley and Robinson, 1990; Patten et al., 2017; Pearce and Robinson, 2010; Regelous et al., 2014). Therefore the metal content of VMS deposits is expected to differ compared to MOR hydrothermal systems.

The chemical composition of volcanic glass from the Troodos ophiolite is different from typical MORB due to elevated As (850 ppb), Sb (78 ppb) and Pb (1.93 ppm) contents, which makes it comparable to subduction related hydrothermal systems such as the Manus Basin (Herzig et al., 1998; Patten et al., 2017; Yeats et al., 2014). In contrast, Se is depleted in the Troodos glass at 119 +/- 53 ppb compared to 243-723 ppb in MORB (Patten et al., 2017). The enrichment of trace metals during magmatic fractionation is not uniform; Cu, Au and Se behave incompatibly during the first stage of crystallisation prior to magnetite saturation (Jenner et al., 2010; Patten et al., 2017). During the second magmatic differentiation stage, (i.e. post magnetite) the melt will be depleted in Cu, Se and Au due to sulfide liquid segregation compared to Zn, As, Sb and Pb showing a typical incompatible behaviour (Patten et al., 2017).

This study highlights the systematic variation of trace metals in VMS ores on a district scale (Figure 2). Deposits of the Solea graben are enriched in Cu, Co, Au and Se (e.g. Skouriotissa or Apliki- Table 6), whilst deposits of the Mitsero graben (e.g. Kokkinoyia or Agrokipia) are enriched in As and Sb (Table 6). We propose that this variation could be due to chemical differences in the composition of the protolithic material in the epidotised zones or the interaction of hydrothermal fluids with different volumes of fresh plutonic igneous rocks (i.e. sheeted dykes/upper plutonics). The extrusive sequence of Troodos is chemically stratified and classified into primitive basaltic upper pillow lavas (UPL) and andesite-dacite lower pillow lavas (LPL) (Gass, 1980; Malpas and Langdon, 1984; Rautenschlein et al., 1985). Hence, an epidosite zone with a higher proportion of more primitive (UPL affinity) dykes would lead to the relative enrichment in Au, Se and Cu, since these elements are enriched in basaltic relative

to an andesitic to dacitic melt (Patten et al., 2017). Given the scale of epidosite zones, estimated at 5-10 km^3 (Jowitt et al., 2012; Patten et al., 2017), local variation could account for the formation of a VMS district that contains elevated Cu, Se and Au. This enrichment is observed in the Solea district (Table 6) that contains the largest (discovered) VMS deposits in the Troodos ophiolite including Skouriotissa and Phoucasa (5.4 Mt at 2.3 % Cu), Phoenix (15 Mt at 0.5 % Cu) and Three Hills (6.2 Mt at 0.4 % Cu), as well as Mavrovouni (15 Mt at 3.8 % Cu) and the smaller Apliki (1.7 Mt at 1.8 % Cu) and Mala deposits (6 Mt at 0.4 % Cu and 12.3 % Zn- exploration report BMG, 2013; Adamides, 2010; Hannington et al., 1998). The deposits of the Mitsero graben are generally of lower tonnage and contain less Cu, such as Mathiatis North (4.5 Mt at 0.17 % Cu) and Sha (1 Mt at 1.9 % Cu; Hannington et al., 1998). We propose a variation in metal source composition or generation of a magmatic volatile phase would be required to account for the systematic variation in metals between the Solea and Mitsero VMS districts.

The spatial association between source rocks and VMS deposits is clearly demonstrated in the southern Troodos Mountains with the occurrence of auriferous VMS deposits (Au grades >3.5 ppm, Au tonnage ≥ 31 t or Au to base metal ratio over unity, Mercier-Langevin et al., 2011). Enrichment of Au at Kalavasos (Table 2) on the southern margin of Troodos (Figure 2) is attributed to a Au enriched source rock. The lava geochemistry of the southern Troodos Mountains are characterised by increased volumes of mafic-ultramafic basaltic to picritic and boninitic affinity lavas (MacLeod and Murton, 1993; Thy, 1987; Thy and Moores, 1988). Patten et al. (2017) show that more primitive basaltic-andesites from Troodos contain higher concentrations of Au (2.1 +/- 0.1 ppb) compared to andesitic glass samples (0.8 ppb). The increased abundance of primitive lavas in the southern Troodos Mountains may be responsible for the Au enrichment in the Kalavasos mines with reported average Au grades of 1.17 ppm (Mercier-Langevin et al., 2011).

Pyrite from Kalavasos has an average Au concentration of 2.1 ppm (n =260, σ = 6.7, max = 40.4 ppm), and is therefore significantly enriched compared to pyrite from the other VMS deposits (average =0.95, median= 0.29 ppm, n = 1062). Like Kalavasos, Mala is located in the southern Troodos Mountains and is enriched in Au averaging 1.7 ppm in pyrite (n= 5, σ= 1.1, max = 2.9- Figure 8) and therefore could also be classified as auriferous.

Keith et al. (2016b) showed that pyrite from the ultramafic-hosted Logatchev vent field on the MAR hosts significant Au as Au^0 inclusions and Au^{1+} in solid solution (Figure 8). Host rock serpentinization causes a H_2S increase in the hydrothermal fluids (Klein and Bach, 2009) enhancing Au solubility and transport potential. It has been shown that serpentinization is a widespread process in the ultramafic domains of the Troodos ophiolite including the southern Troodos Mountains, similar to oceanic core

complexes on the modern seafloor (Nuriel et al., 2009). Therefore, it is likely that Kalavasos and Mala are enriched in Au as a function of both source rock Au content and enhanced Au solubility in H_2S rich fluids (William-Jones and Heinrich, 2005).

In modern mafic-ultramafic hosted SMS deposits that exhibit a Au enrichment, such as the Semenov 2 hydrothermal field (average 65 ppm Au- bulk ore), an additional source is hypothesised to explain the Au enrichment (Melekestseva et al., 2017). Whilst we realise that the Au content of Troodos VMS is significantly less than the 65 ppm average for Semenov 2; Melekestseva et al. (2017) also reported elevated concentrations of Se, Te, Cu and Au which they find inconsistent with a purely basaltic-ultramafic source. Instead Melekestseva et al. (2017) prefer an additional metal contribution from a fluid source via a magmatic volatile influx into the hydrothermal system.

5.4 Magmatic volatile fluid flux to the hydrothermal system

In addition to variation in host rock chemistry a direct magmatic influx through volatiles into the hydrothermal system could explain the enrichment in magmatophile trace elements in the Solea domain (Layton-Matthews et al., 2013; de Ronde et al., 2003, 2005; Yang and Scott, 2002). The Se/S ratio of pyrite($Se/S*10^6$) can be used as a proxy for the influx of magmatic volatiles into VMS hydrothermal systems (Layton-Matthews et al., 2008, 2013). For example, elevated Se/S ratios in pyrite from the Bornite Zone at Kidd Creek of >20,000 are attributed to and associated with a late magmatic influx (Hannington et al., 1999). Selenium/S ratios of >500 represent an increased magmatic volatile component in VMS systems and all values for sediment-free ridges (back-arc and MOR), such as Troodos (Robertson and Xenophontos, 1993) are predicted to fall below 1500 (Figure 9) (Layton-Matthews et al., 2008). However, the Se/S ratios in pyrite from this study range from 1.6 to 9240 suggesting a variable magmatic volatile influx into the Troodos hydrothermal systems (Figure 9).

The structural domains of Solea and Mitsero display systematically different pyrite Se/S ratios (Appendix A6). The Solea graben shows the highest average Se/S ratio at 581 (max= 9280, n= 427) and the Mitsero graben the lowest at 31 (max= 640 n=100- Figure 9). This systematic variation between these two structural domains may be due to a variable magmatic volatile influx with the Solea graben experiencing the highest magmatic contribution. Keith et al. (2016a) reported $\delta^{34}S$ isotope values in pyrite (mineral separates) from Skouriotissa that are skewed towards light magmatic (Troodos 0-1 ‰: Alt, 1994; Vibetti, 1993) $\delta^{34}S$ values at -1.6 ‰. This is significantly lighter than average $\delta^{34}S$ values quoted by Alt (1994) for other Troodos VMS sulfides of +4 to +7 ‰. Herzig et al. (1998) demonstrate large variations in $\delta^{34}S$ composition in hydrothermal sulfides from the Valu Fa Ridge (Manus Basin). They show that the $\delta^{34}S$ composition of SMS pyrite is directly linked to the spreading evolution of the

Valu Fa Ridge where vent fields separated by just 30 km are characterised by extreme $\delta^{34}S$ variations from -7.3 ‰ at Hine Hina to + 10.9 ‰ at Vai Lili (Herzig et al., 1998). Such variations can be attributed to local spreading centre evolution with Hine Hina forming proximal to a magmatic source and thus experiencing an increased ingress of magmatic derived volatiles with a $\delta^{34}S$ isotopic signature lighter than typical for a seawater dominated system. Herzig et al., (1998) suggest the reduction of magmatic SO_2 to H_2S form shallow magma conduits and decreased seawater ingress to explain the extremely light $\delta^{34}S$ values at Hine Hina.

Whilst the Se/S ratio in pyrite is only a proxy for the magmatic influx and detailed $\delta^{34}S$ analyses are needed to confirm these results, the systematic variation in Se/S between the Solea and Mitsero graben can be preliminary linked to the spreading evolution of the Troodos ophiolite. Evidence suggest that the Solea graben represents a full spreading ridge whilst Mitsero formed during migration of spreading between two rift structures, most likely as a propagating ridge tip (Everdingen et al., 1995; Hurst et al., 1994; Varga and Moores, 1985). The lower average Se/S ratio of 31 (n=100) (Figure 9) for Mitsero supports the structural observation that Mitsero formed through extension of older oceanic crust in an off-axis position (see Everdingen et al., 1995). In this scenario, the magmatic volatile influx to the VMS system would be diminished and the pyrite Se/S ratio would be lower relative to Solea; a 'full' magmatic spreading centre that experienced higher magmatic volatile input.

The Troodos lava geochemistry is different to MORB showing an enrichment in volatile elements and H_2O (2-4.5 wt.% H_2O- Fonseca et al., 2017; Patten et al., 2017). Highly saline quartz-and epidote hosted fluid inclusions (T_H=400-500˚C, 36-61 wt.% NaCl equivalent) provide further evidence for a magmatic volatile contribution to the Troodos hydrothermal systems and associated VMS deposits (Kelley et al., 1992, 1993; Kelley and Robinson, 1990). The brine rich inclusions are concentrated in plagiogranites and associated epidosites, the residual products of fractional crystallisation or partial melting of hydrated lower crustal gabbroic rocks (Grimes et al., 2013; Freund et al., 2014). Plagiogranites generally form below the penetration depth of seawater, with only the upper most crack front or contact aureole showing evidence of hydrothermal alteration (epidote veins etc.), therefore, brine and associated volatiles are only partly accessible to the hydrothermal fluid (Gillis and Roberts, 1999; Gillis and Coogan, 2002; Kelley et al., 1992; Vibetti, 1993). Any magma derived brine must breach the boundary conductive layer in order to be accessible to the hydrothermal system otherwise metals may not be transferred from the magmatic to hydrothermal environment (Gillis and Roberts, 1999- Figure 10). The repeated non-steady state injection of high level magma conduits would lead to the temporal migration of the boundary conductive layer (Figure 10) (Gillis and Roberts, 1999; Kelley and Robinson, 1990). The migration of the boundary and crucially generation of extensive fracturing would allow hydrothermal fluids to penetrate and incorporate magmatic volatile rich brines (and metals)

from the upper plutonics. Thus, we hypothesis that this magmatophile trace element signature is preserved in the Troodos VMS deposits as a systematic variation in Se/S and the distribution of magmatophile elements, such as Te, Se, Bi and Cu between the Solea and Mitsero graben (Figures 8, 9 and 10). At Solea the boundary conductive layer is subject to multiple magma injections, i.e. a full spreading ridge, suggesting a higher fracture density due to repetitive magma injection and penecontemporaneous graben formation leading to an increased probability of brine migration from the magmatic to the hydrothermal system (Figure 10). In contrast the boundary would be less mobile at Mitsero and volatile enrichment is less likely to occur leading to a depletion in magmatophile elements and lower Se/S ratios in pyrite relative to Solea (Figure 10).

6. Summary and conclusions

This study provides the first extensive high-resolution in situ data for trace elements in sulfide minerals for the VMS deposits of the Troodos ophiolite allowing us to study regional scale ore-forming processes related to spreading centre evolution. Spot and line analyses by LA-ICP-MS show that the distribution of trace elements in hydrothermal sulfides from various Troodos VMS deposits are extremely variable on both a deposit and a regional scale, i.e. between structural domains. Minor correlation of most trace elements on a deposit scale suggests that local changes in physicochemical factors, such as fluid temperature affect the trace element distribution in a highly dynamic environment. In particular, Se is preferentially incorporated in chalcopyrite rich ore that is more common in the lower VMS stratigraphy. Upon cooling to <260˚C chalcopyrite precipitation ceased, leading to a reduction in Se uptake in the lower VMS stratigraphy and the preferential incorporation of Se into pyrite in the upper near seafloor sections of the deposit.

Time resolved LA-ICP-MS analysis demonstrates that some trace elements are incorporated in sulfides via lattice substitution in solid solution (e.g., Se, As, Sb), whilst others likely occur as both micro- and nanoscale inclusions or in solid solution (e.g. Te). Discrimination diagrams demonstrate the importance of As in incorporating elements with large covalent radii such as Te into the pyrite lattice. Colloform pyrite acts as a reservoir for Mo, Sb and Au, while euhedral pyrite exhibits an enrichment in Co, Te, Bi and Se. The variation in trace element composition between the two pyrite types is attributed to the rapid, disequilibrium precipitation of colloform pyrite relative to euhedral pyrite. Chalcopyrite from the stockwork zone contains elevated Co, Ni and Se compared to pyrite which reflects the enhanced substitution potential of Se, Ni and Co in chalcopyrite relative to pyrite.

Systematic variations of the Se/S ratio in pyrite on a graben scale coupled with our current understanding of the spreading evolution of Troodos suggest a heterogeneous source of trace metals in the Troodos VMS deposits. Variable magmatic volatile influx related to a) ‘magma’ volume, b)

migration of the magmatic-hydrothermal crack front and brine liberation, or c) a variation in protolith metal concentration are proposed as mechanisms to explain regional scale variations in VMS geochemistry.

Compared to typical MOR hydrothermal systems, VMS deposits of the Troodos ophiolite and in particular those of Solea (Mala, Apliki and Skouriotissa) are enriched in magmatophile elements derived from a volatile source. We hypothesise a variable magmatic volatile influx linked with the subduction zone nature of the Troodos ophiolite that leads to the enrichment of Te, Se, Bi, and Cu. We propose that the Troodos hydrothermal systems and associated sulfide deposits are similar to those of the Valu Fa Ridge, where magmatic volatile signatures vary on a 30 km scale leading to distinct magmatophile rich trace element profiles in seafloor massive sulfides that experienced variable amounts of magmatic volatile influx. This raises the question whether Cyprus-type VMS deposits can still be considered representative as true ancient analogues for modern active hydrothermal systems at sediment-free mid-ocean ridge spreading centres.

Acknowledgements

This research was supported by the Natural Environmental Research Council (NERC) under the tellurium and selenium cycling and supply grant NE/M010848/1. The authors thank Prof. Franco Pirajno for the efficient editorial handling of this manuscript and Dr. Artur Deditius and an anonymous reviewer for comments that improved the quality of this manuscript. Dr. Andreas Zissimos and the Director of the Geological Survey Department Dr. Costas Constantinou are thanked for their continued support and enthusiasm towards this project. Dr. Helene Brätz is thanked for help with the LA-ICPMS analyses at Erlangen University. We also thank Hellenic Copper Mines for allowing access to the Apliki and Skouriotissa mines and Dr. Michael Green, Ifigenia Gavriel and Lazaros Georgiou for their assistance and advice in the field.

7. References

Abraitis, P.K., Pattrick, R.A.D., Vaughan, D.J., 2004. Variations in the compositional, textural and electrical properties of natural pyrite: a review. International Journal of Mineral Processing 74, 41–59. https://doi.org/10.1016/j.minpro.2003.09.002

Adamides, N.., 2010. Mafic-dominated volcanogenic sulphide deposits in the Troodos ophiolite, Cyprus Part 2- A review of genetic models and guides for exploration. Applied Earth Science 119, 193–204.

Allerton, S., Vine, F.., 1991. Spreading evolution of the Troodos ophiolite, Cyprus. Geology 19, 637–640.

Alt, J.C., 1994. A sulfur isotopic profile through the Troodos ophiolite, Cyprus: Primary composition and the effects of seawater hydrothermal alteration. Geochimica et Cosmochimica Acta 58, 1825–1840. https://doi.org/10.1016/0016-7037(94)90539-8

Auclair, G., Fouquet, Y., Bohn, M., 1987. Distribution of selenium in high temperature hydrothermal sulfide deposits at 13 degrees north, East Pacific Rise. Can. Mineral. 25, 577–587.

Barrie, C.T., D Hannington, M., 1999. Classification of Volcanic-Associated Massive Sulfide Deposits Based on Host-Rock Composition, in: Rev. Econ. Geo. pp. 1–11.

Berkenbosch, H.A., Ronde, C.E.J. de, Gemmell, J.B., McNeill, A.W., Goemann, K., 2012. Mineralogy and Formation of Black Smoker Chimneys from Brothers Submarine Volcano, Kermadec Arc. Economic Geology 107, 1613–1633. https://doi.org/10.2113/econgeo.107.8.1613

Bethke, P.M., Barton, P.B., 1971. Distribution of some minor elements between coexisting sulfide minerals. Econ. Geol. 66, 140–163. https://doi.org/10.2113/gsecongeo.66.1.140

Boschen, R.E., Rowden, A.A., Clark, M.R., Gardner, J.P.A., 2013. Mining of deep-sea seafloor massive sulfides: A review of the deposits, their benthic communities, impacts from mining, regulatory frameworks and management strategies. Ocean & Coastal Management 84, 54–67. https://doi.org/10.1016/j.ocecoaman.2013.07.005

Butler, I.B., Nesbitt, R.W., 1999. Trace element distributions in the chalcopyrite wall of a black smoker chimney: insights from laser ablation inductively coupled plasma mass spectrometry (LA–ICP–MS). Earth Planet. Sci. Lett. 167, 335–345.

Chouinard, A., Paquette, J., Williams-Jones, A.E., 2005. Crystallographic Controls on Trace-Element Incorporation in Auriferous Pyrite from the Pascua Epithermal High-Sulfidation Deposit, Chile–Argentina. Can Mineral 43, 951–963. https://doi.org/10.2113/gscanmin.43.3.951

Constantinou, G., 1980. Metalogenesis associated with Troodos ophiolite, in: Ophiolites, Proceedings: International Ophiolite Synposium, Cyprus 1979. The Geological Survey Department, Ministry of Agriculture and Natural Resources, Nicosia, Cyprus, pp. 663–674.

Cook, N.J., Ciobanu, C.L., Danyushevsky, L.V., Gilbert, S., 2011. Minor and trace elements in bornite and associated Cu–(Fe)-sulfides: A LA-ICP-MS studyBornite mineral chemistry. Geochimica et Cosmochimica Acta 75, 6473–6496. https://doi.org/10.1016/j.gca.2011.08.021

Cook, N.J., Ciobanu, C.L., Pring, A., Skinner, W., Shimizu, M., Danyushevsky, L., Saini-Eidukat, B., Melcher, F., 2009. Trace and minor elements in sphalerite: A LA-ICPMS study. Geochimica et Cosmochimica Acta 73, 4761–4791. https://doi.org/10.1016/j.gca.2009.05.045

Cordero, B., Gómez, V., Platero-Prats, A.E., Revés, M., Echeverría, J., Cremades, E., Barragán, F., Alvarez, S., 2008. Covalent radii revisited. Dalton Trans. 0, 2832–2838.

Cox, D.., Singer, D.A., 1986. Mineral Deposit Models- US Geological Survey Bulletin 1693, 1st ed, US Geological Survey Bulletin. U.S Geological Survey.

Damm, K.L.V., 1990. Seafloor Hydrothermal Activity: Black Smoker Chemistry and Chimneys. Annual Review of Earth and Planetary Sciences 18, 173–204. https://doi.org/10.1146/annurev.ea.18.050190.001133

Deditius, A.P., Reich, M., Kesler, S.E., Utsunomiya, S., Chryssoulis, S.L., Walshe, J., Ewing, R.C., 2014. The coupled geochemistry of Au and As in pyrite from hydrothermal ore deposits. Geochimica et Cosmochimica Acta 140, 644–670. https://doi.org/10.1016/j.gca.2014.05.045

Deditius, A.P., Utsunomiya, S., Reich, M., Kesler, S.E., Ewing, R.C., Hough, R., Walshe, J., 2011. Trace metal nanoparticles in pyrite. Ore Geology Reviews, Nanogeoscience in ore systems research: principles, methods, and applications 42, 32–46. https://doi.org/10.1016/j.oregeorev.2011.03.003

Deditius, A.P., Utsunomiya, S., Renock, D., Ewing, R.C., Ramana, C.V., Becker, U., Kesler, S.E., 2008. A proposed new type of arsenian pyrite: Composition, nanostructure and geological significance. Geochimica et Cosmochimica Acta 72, 2919–2933. https://doi.org/10.1016/j.gca.2008.03.014

Deditius, A.P., Reich, M., 2016. Constraints on the solid solubility of Hg, Tl, and Cd in arsenian pyrite. Am. Mineral. 101, 1451–1459.

de Ronde, C.E., Faure, K., Bray, C.J., Chappell, D.A., Wright, I.C., 2003. Hydrothermal fluids associated with seafloor mineralization at two southern Kermadec arc volcanoes, offshore New Zealand. Miner. Deposita 38, 217–233.

de Ronde, C.E.J., Hannington, M.D., Stoffers, P., Wright, I.C., Ditchburn, R.G., Reyes, A.G., Baker, E.T., Massoth, G.J., Lupton, J.E., Walker, S.L., Greene, R.R., Soong, C.W.R., Ishibashi, J., Lebon, G.T., Bray, C.J., Resing, J.A., 2005. Evolution of a Submarine Magmatic-Hydrothermal System: Brothers Volcano, Southern Kermadec Arc, New Zealand. Econ. Geol. 100, 1097–1133.

de Ronde, C.E.J., Massoth, G.J., Butterfield, D.A., Christenson, B.W., Ishibashi, J., Ditchburn, R.G., Hannington, M.D., Brathwaite, R.L., Lupton, J.E., Kamenetsky, V.S., Graham, I.J., Zellmer, G.F., Dziak, R.P., Embley R.W., Dekov V.M., Munnik F., Lahr, J., Evans, J.E. and Takai, K., 2011 Submarine hydrothermal activity and gold rich mineralization at Brothers Volcano, Kermadec Arc, New Zealand. Mineral Dep, 46, 541-584.

Everdingen, D.A. van, Cawood, P.A., Everdingen, D.A. van, Cawood, P.A., 1995. Dyke domains in the Mitsero graben, Troodos ophiolite, Cyprus: an off-axis model for graben formation at a spreading centre. Journal of the Geological Society 152, 923–932. https://doi.org/10.1144/GSL.JGS.1995.152.01.07

Fonseca, R.O.C., Kirchenbaur, M., Ballhaus, C., Münker, C., Zirner, A., Gerdes, A., Heuser, A., Botcharnikov, R., Lenting, C., 2017. Fingerprinting fluid sources in Troodos ophiolite complex orbicular glasses using high spatial resolution isotope and trace element geochemistry. Geochimica et Cosmochimica Acta 200, 145–166. https://doi.org/10.1016/j.gca.2016.12.012

Franklin, J.M., Gibson, H.L., Jonasson, I.R., and Galley, A.G. 2005. Volcanogenic Massive Sulfide Deposits. P.p 523-560. In: Economic Geology 100th Anniversary Volume (Hedenquist, J.W., Thompson, J.F.H., Goldfarb, R.J., and Richards, J.P., eds.), Soc. of Econ. Geol.

Franklin J.M., Sangster D.M., and Lydon, J.W., 1981, Volcanic-associated massive sulfide deposits: Economic Geology 75th Anniversary Volume, p. 485-627.

Freund, S., Haase, K.M., Keith, M., Beier, C., Garbe-Schönberg, D., 2014. Constraints on the formation of geochemically variable plagiogranite intrusions in the Troodos Ophiolite, Cyprus. Contrib. Mineral. Petrol. 167, 978.

Galley, A., Hannington, M., Jonasson, I., 2007. Volcanogenic Massive Sulphide Deposits. Mineral Deposits of Canada Special publication No. 5, 141–161.

Gass, I.G., 1980. The Troodos massif: Its role in the unravelling of the ophiolite problem and its significance in the understanding of constructive plate margin processes, in: Ophiolites, Proceedings: International Ophiolite Symposium, Cyprus 1979. The Geological Survey Department, Ministry of Agriculture and Natural Resources, Nicosia, Cyprus, pp. 23–35.

Gass, I.G., Smewing, J.D., 1973. Intrusion, Extrusion and Metamorphism at Constructive Margins: Evidence from the Troodos Massif, Cyprus. Nature 242, 26–29.

Gena, K., Chiba, H., Kase, K., Nakashima, K., Ishiyama, D., 2013. The Tiger Sulfide Chimney, Yonaguni Knoll IV Hydrothermal Field, Southern Okinawa Trough, Japan: The First Reported Occurrence of Pt-Cu-Fe-Bearing Bismuthinite and Sn-Bearing Chalcopyrite in an Active Seafloor Hydrothermal System. Resour. Geol. 63, 360–370. https://doi.org/10.1111/rge.12015

Genna, D., Gaboury, D., 2015. Deciphering the Hydrothermal Evolution of a VMS System by LA-ICP-MS Using Trace Elements in Pyrite: An Example from the Bracemac-McLeod Deposits, Abitibi, Canada, and Implications for Exploration. Economic Geology 110, 2087–2108. https://doi.org/10.2113/econgeo.110.8.2087

George, L.L., Cook, N.J., Ciobanu, C.L., 2016. Partitioning of trace elements in co-crystallized sphalerite–galena–chalcopyrite hydrothermal ores. Ore Geol. Rev. C, 97–116. https://doi.org/10.1016/j.oregeorev.2016.02.009

George, L.L., Cook, N.J., Crowe, B.B.P., Ciobanu, C.L., 2018. Trace elements in hydrothermal chalcopyrite. Mineral. Mag. 1–61. https://doi.org/10.1180/minmag.2017.081.021

Gillis, K.M., Roberts, M.D., 1999. Cracking at the magma–hydrothermal transition: evidence from the Troodos Ophiolite, Cyprus. Earth Planet. Sci. Lett. 169, 227–244.

Gillis, K.M., Coogan, L.A., 2002. Anatectic Migmatites from the Roof of an Ocean Ridge Magma Chamber. J. Petrol. 43, 2075–2095

Gregory, D. D., Large, R. R., Halpin, J. A., Baturina, E. L., Lyons, T. W., Wu, S., Danyushevsky, L., Sack,P. J., Chappaz, A., and Maslennikov, V. V. (2015a) Trace Element Content of Sedimentary Pyrite in Black Shales.Econ. Geol. 110, 1389-1410.

Grimes, C.B., Ushikubo, T., Kozdon, R., Valley, J.W., 2013. Perspectives on the origin of plagiogranite in ophiolites from oxygen isotopes in zircon. Lithos 179, 48–66.

Hannington, M., Jamieson, J., Monecke, T., Petersen, S., Beaulieu, S., 2011. The abundance of seafloor massive sulfide deposits. Geology. 39, 1155-1158

Hannington, M.D., Barrie, C.T., Bleeker, W., 1999. The Giant Kidd Creek Volcanogenic Massive Sulfide Deposit, Western Abitibi Subprovince, Canada: Summary and Synthesis, in: Hannington, M.D., Barrie, C.T. (Eds.), The Giant Kidd Creek Volcanogenic Massive Sulfide Deposit, Western Abitibi Subprovince, Canada. Soc. of Econ Geol.

Hannington, M.D., de Ronde, C.D.J., Petersen, S., 2005. Sea-floor tectonics and submarine hydrothermal systems, in: Hedenquist, J.W., Thompson, J.F.H., Goldfarb, R.J., Richards, J.P. (Eds.), Economic Geology 100th Anniversary Volume. Soc. of Econ. Geol., Littelton, Colorado, USA, pp. 111–141.

Hannington, M.D., Galley, A., Gerzig, P., Petersen, S., 1998. Comparison of the TAG mound and stockwork complex with Cyprus-type massive sulfide deposits. Proc. Ocean Drill. Program Sci. Results 158, 389–415.

Hannington, M.D., Herzig, P.M., Alt, J.C., 1990. The distribution of gold in sub-seafloor stockwork mineralization from DSDP hole 504B and the Agrokipia B deposit, Cyprus. Can. J. Earth Sci. 27, 1409–1417.

Herzig, P.M., Hannington, M.D., 1995. Polymetallic massive sulfides at the modern seafloor a review. Ore Geology Reviews 10, 95–115. https://doi.org/10.1016/0169-1368(95)00009-7

Herzig, P.M., Hannington, M.D., Jr, A.A., 1998a. Sulfur isotopic composition of hydrothermal precipitates from the Lau back-arc: implications for magmatic contributions to seafloor hydrothermal systems. Mineral. Deposita 33, 226–237. https://doi.org/10.1007/s001260050143

Herzig, P.M., Hannington, M.D., Jr, A.A., 1998b. Sulfur isotopic composition of hydrothermal precipitates from the Lau back-arc: implications for magmatic contributions to seafloor

hydrothermal systems. Mineral. Deposita 33, 226–237. https://doi.org/10.1007/s001260050143

Humphris, S.E., Cann, J.R., 2000. Constraints on the energy and chemical balances of the modern TAG and ancient Cyprus seafloor sulfide deposits. J. Geophys. Res. 105, 28477–28488. https://doi.org/10.1029/2000JB900289

Humphris, S.E., Herzig, P.M., Miller, D.J., Alt, J.C., Becker, K., Brown, D., Brügmann, G., Chiba, H., Fouquet, Y., Gemmell, J.B., Guerin, G., Hannington, M.D., Holm, N.G., Honnorez, J.J., Iturrino, G.J., Knott, R., Ludwig, R., Nakamura, K., Petersen, S., Reysenbach, A.-L., Rona, P.A., Smith, S., A. A, S., Tivey, M.K., Zhao, X., 1995. The internal structure of an active sea-floor massive sulphide deposit. Nature 377, 713–716. https://doi.org/10.1038/377713a0

Humphris, S.E., Klein, F., 2018. Progress in Deciphering the Controls on the Geochemistry of Fluids in Seafloor Hydrothermal Systems. Annual Review of Marine Science 10, 315–343. https://doi.org/10.1146/annurev-marine-121916-063233

Hurst, S.D., Moores, E.M., Varga, R.J., 1994. Structural and geophysical expression of the Solea graben, Troodos Ophiolite, Cyprus. Tectonics 13, 139–156. https://doi.org/10.1029/93TC02066

Huston, D.L., Sie, S.H., Suter, G.F., Cooke, D.R., Both, R.A., 1995. Trace elements in sulfide minerals from eastern Australian volcanic-hosted massive sulfide deposits; Part I, Proton microprobe analyses of pyrite, chalcopyrite, and sphalerite, and Part II, Selenium levels in pyrite; comparison with delta ^{34} S values and implications for the source of sulfur in volcanogenic hydrothermal systems. Economic Geology 90, 1167–1196. https://doi.org/10.2113/gsecongeo.90.5.1167

Jowitt, S.M., Jenkin, G.R.T., Coogan, L.A., Naden, J., 2012. Quantifying the release of base metals from source rocks for volcanogenic massive sulfide deposits: Effects of protolith composition and alteration mineralogy. Journal of Geochemical Exploration 118, 47–59. https://doi.org/10.1016/j.gexplo.2012.04.005

Jenner, F.E., O'Neill, H.S.C., Arculus, R.J., Mavrogenes, J.A., 2010. The Magnetite Crisis in the Evolution of Arc-related Magmas and the Initial Concentration of Au, Ag and Cu. J. Petrol. 51, 2445–2464.

Keith, M., Haase, K.M., Klemd, R., Krumm, S., Strauss, H., 2016a. Systematic variations of trace element and sulfur isotope compositions in pyrite with stratigraphic depth in the Skouriotissa volcanic-hosted massive sulfide deposit, Troodos ophiolite, Cyprus. Chemical Geology. https://doi.org/10.1016/j.chemgeo.2015.12.012

Keith, M., Häckel, F., Haase, K.M., Schwarz-Schampera, U., Klemd, R., 2016b. Trace element systematics of pyrite from submarine hydrothermal vents. Ore Geol. Rev. 72, 728–745.

Keith, M., Smith, D.J., Jenkin, G.R.T., Holwell, D.A., Dye, M.D., 2018. A review of Te and Se systematics in hydrothermal pyrite from precious metal deposits: Insights into ore-forming processes. Ore Geology Reviews. https://doi.org/10.1016/j.oregeorev.2017.07.023

Kelley, D.S., Gillis, K.M., Thompson, G., 1993. Fluid evolution in submarine magma-hydrothermal systems at the Mid-Atlantic Ridge. J. Geophys. Res. Solid Earth 98, 19579–19596.

Kelley, D.S., Robinson, P.T., 1990. Development of a brine-dominated hydrothermal system at temperatures of 400–500°C in the upper level plutonic sequence, Troodos ophiolite, Cyprus. Geochim. Cosmochim. Acta 54, 653–661.

Kelley, D.S., Robinson, P.T., Malpas, J.G., 1992. Processes of brine generation and circulation in the oceanic crust: Fluid inclusion evidence from the Troodos Ophiolite, Cyprus. J. Geophys. Res. Solid Earth 97, 9307–9322.

Klein, F., Bach, W., 2009. Fe–Ni–Co–O–S Phase Relations in Peridotite–Seawater Interactions. J. Petrol. 50, 37–59.

Kelley, D.S., Robinson, P.T., Malpas, J.G., 1992. Processes of brine generation and circulation in the oceanic crust: Fluid inclusion evidence from the Troodos Ophiolite, Cyprus. J. Geophys. Res. 97, 9307–9322. https://doi.org/10.1029/92JB00520

Koschinsky, A., Garbe-Schönberg, D., Sander, S., Schmidt, K., Gennerich, H.-H., Strauss, H., 2008. Hydrothermal venting at pressure-temperature conditions above the critical point of seawater, 5°S on the Mid-Atlantic Ridge. Geology 36, 615–618. https://doi.org/10.1130/G24726A.1

Kristall, B., Nielsen, D., Hannington, M.D., Kelley, D.S., Delaney, J.R., 2011. Chemical microenvironments within sulfide structures from the Mothra Hydrothermal Field: Evidence from high-resolution zoning of trace elements. Chem. Geol. 290, 12–30.

Large, R.R., Danyushevsky, L., Hollit, C., Maslennikov, V., Meffre, S., Gilbert, S., Bull, S., Scott, R., Emsbo, P., Thomas, H., Singh, B., Foster, J., 2009. Gold and Trace Element Zonation in Pyrite Using a Laser Imaging Technique: Implications for the Timing of Gold in Orogenic and Carlin-Style Sediment-Hosted Deposits. Econ. Geol. 104, 635–668. https://doi.org/10.2113/gsecongeo.104.5.635

Layton-Matthews, D., Leybourne, M.I., Peter, J.M., Scott, S.D., Cousens, B., Eglington, B.M., 2013. Multiple sources of selenium in ancient seafloor hydrothermal systems: Compositional and Se, S, and Pb isotopic evidence from volcanic-hosted and volcanic-sediment-hosted massive

sulfide deposits of the Finlayson Lake District, Yukon, Canada. Geochimica et Cosmochimica Acta 117, 313–331. https://doi.org/10.1016/j.gca.2013.05.002

Layton-Matthews, D., Peter, J.M., Scott, S.D., Leybourne, M.I., 2008. Distribution, Mineralogy, and Geochemistry of Selenium in Felsic Volcanic-Hosted Massive Sulfide Deposits of the Finlayson Lake District, Yukon Territory, Canada. Economic Geology 103, 61–88. https://doi.org/10.2113/gsecongeo.103.1.61

Lüders, V., Banks, D.A., Halbach, P., 2002. Extreme Cl/Br and δ37Cl isotope fractionation in fluids of modern submarine hydrothermal systems. Miner. Deposita 37, 765–771.

MacLeod, C.J., Murton, B.J., 1993. Structure and tectonic evolution of the Southern Troodos Transform Fault Zone, Cyprus. Geological Society, London, Special Publications 76, 141–176. https://doi.org/10.1144/GSL.SP.1993.076.01.07

MacLeod, C.J., Robertson, A.H.F., Allerton, S., Browning, P., Gass, I.G., Taylor, R.N., Vine, F.J., Xenophontos, C., 1992. Comment [on "Tectonic evolution of the Troodos ophiolite within the Tethyan framework" by Y. Dilek, P. Thy, E. M. Moores, and T. W. Ramsden]. Tectonics 11, 910–915. https://doi.org/10.1029/92TC00458

Malpas, J., Langdon, G., 1984. Petrology of the Upper Pillow Lava suite, Troodos ophiolite, Cyprus. Geol. Soc. Lond. Spec. Publ. 13, 155–167.

Martin, A.J., McDonald, I, MaccLeod C.J., McFall, K, Prichard, H.M. 2018. The extreme enrichment of Se in the Apliki Cyprus-type VMS deposit, Troodos, Cyprus. Mineral. Mag. 82(3), 1-28. 10.1180/mgm.2018.81

Maslennikov, V.V., Maslennikova, S.P., Large, R.R., Danyushevsky, L.V., 2009. Study of Trace Element Zonation in Vent Chimneys from the Silurian Yaman-Kasy Volcanic-Hosted Massive Sulfide Deposit (Southern Urals, Russia) Using Laser Ablation-Inductively Coupled Plasma Mass Spectrometry (LA-ICPMS). Economic Geology 104, 1111–1141. https://doi.org/10.2113/gsecongeo.104.8.1111

Maslennikov, V.V., Maslennikova, S.P., Large, R.R., Danyushevsky, L.V., Herrington, R.J., Stanley, C.J., 2012. Tellurium-bearing minerals in zoned sulfide chimneys from Cu-Zn massive sulfide deposits of the Urals, Russia. Mineral. Petrol. 107, 67–99. https://doi.org/10.1007/s00710-012-0230-x

Maslennikov, V.V., Maslennikova, S.P., Large, R.R., Danyushevsky, L.V., Herrington, R.J., Ayupova, N.R., Zaykov, V.V., Lein, A.Y., Tseluyko, A.S., Melekestseva, I.Y., Tessalina, S.G., 2017. Chimneys in Paleozoic massive sulfide mounds of the Urals VMS deposits: Mineral and trace element comparison with modern black, grey, white and clear smokers. Ore Geology

Reviews, Overview of mineral deposits in the Urals 85, 64–106. https://doi.org/10.1016/j.oregeorev.2016.09.012

Melekestseva, I.Y., Maslennikov, V.V., Tret'yakov, G.A., Nimis, P., Beltenev, V.E., Rozhdestvenskaya, I.I., Maslennikova, S.P., Belogub, E.V., Danyushevsky, L., Large, R., Yuminov, A.M., Sadykov, S.A., 2017. Gold- and Silver-Rich Massive Sulfides from the Semenov-2 Hydrothermal Field, 13°31.13'N, Mid-Atlantic Ridge: A Case of Magmatic Contribution? Economic Geology 112, 741–773. https://doi.org/10.2113/econgeo.112.4.741

Mercier-Langevin, P., Hannington, M.D., Dubé, B., Bécu, V., 2011. The gold content of volcanogenic massive sulfide deposits. Miner Deposita 46, 509–539. https://doi.org/10.1007/s00126-010-0300-0

Metz, S., Trefry, J.H., 2000. Chemical and mineralogical influences on concentrations of trace metals in hydrothermal fluids. Geochimica et Cosmochimica Acta 64, 2267–2279. https://doi.org/10.1016/S0016-7037(00)00354-9

Miyashiro, A. (1973). The Troodos Ophiolitic Complex was probably formed in an island arc. Earth and Planetary Sciene Letters. 19, 218-224.

Monecke, T., Petersen, S., Hannington, M.D., 2014. Constraints on Water Depth of Massive Sulfide Formation: Evidence from Modern Seafloor Hydrothermal Systems in Arc-Related Settings. Economic Geology 109, 2079–2101. https://doi.org/10.2113/econgeo.109.8.2079

Moores, E.M., Vine, F., 1971. The Troodos Massif, Cyprus and other ophiolites as oceanic crust: evaluation and implication. Phil. Trans. Roy. Soc. of Lon. 268, 443–466.

Moores, E.M., Varga, R.J., Verosub, K.L., Ramsden, T.W., 1990. Regional structure of the Troodos dyke complex. In: Malpas, J., Moores, E.M., Panayiotou, A., Xenophontos, C. (Eds.), Troodos 1987: Ophiolites, Oceanic Crustal Analogues. Geol. Surv. Dept. Cyprus, Nicosia, pp. 27–35.

Moss, R., Scott, S.D., 2001. Geochemistry and Mineralogy of Gold-Rich Hydrothermal Precipitates from the Eastern Manus Basin, Papua New Guinea. Can Mineral 39, 957–978. https://doi.org/10.2113/gscanmin.39.4.957

Mottl, M.J., Holland, H.D., 1978. Chemical exchange during hydrothermal alteration of basalt by seawater—I. Experimental results for major and minor components of seawater. Geochimica et Cosmochimica Acta 42, 1103–1115. https://doi.org/10.1016/0016-7037(78)90107-2

Nesbitt, H.W., Muir, I.J., Prarr, A.R., 1995. Oxidation of arsenopyrite by air and air-saturated, distilled water, and implications for mechanism of oxidation. Geochimica et Cosmochimica Acta 59, 1773–1786. https://doi.org/10.1016/0016-7037(95)00081-A

Nuriel, P., Katzir, Y., Abelson, M., Valley, J.W., Matthews, A., Spicuzza, M.J., Ayalon, A., 2009. Fault-related oceanic serpentinization in the Troodos ophiolite, Cyprus: Implications for a fossil

oceanic core complex. Earth and Planetary Science Letters 282, 34–46. https://doi.org/10.1016/j.epsl.2009.02.029

Patten, C.G.C., Pitcairn, I.K., Teagle, D.A.H., 2017. Hydrothermal mobilisation of Au and other metals in supra-subduction oceanic crust: Insights from the Troodos ophiolite. Ore Geology Reviews 86, 487–508. https://doi.org/10.1016/j.oregeorev.2017.02.019

Patten, C.G.C., Pitcairn, I.K., Teagle, D.A.H., Harris, M., 2016. Mobility of Au and related elements during the hydrothermal alteration of the oceanic crust: implications for the sources of metals in VMS deposits. Miner Deposita 51, 179–200. https://doi.org/10.1007/s00126-015-0598-8

Pearce, J.A., Robinson, P.T., 2010. The Troodos ophiolitic complex probably formed in a subduction initiation, slab edge setting. Gondwana Research, A Tribute to Miyashiro 18, 60–81. https://doi.org/10.1016/j.gr.2009.12.003

Pearce, J.A., Lippard, S.J., & Roberts, S. (1984). Characteristics and tectonic significance of supra-subduction zone ophiolites. P.p. 77-96. In*:* Ophiolites and Oceanic Lithosphere (Gass, I.G.; Lippard, S.J. & Shelton, A.W. eds.). Geological Society of London, No. 13

Pokrovski, G.S., Kara, S., Roux, J., 2002. Stability and solubility of arsenopyrite, FeAsS, in crustal fluids. Geochimica et Cosmochimica Acta 66, 2361–2378. https://doi.org/10.1016/S0016-7037(02)00836-0

Prichard, H.M., Knight, R.D., Fisher, P.C., McDonald, I., Zhou, M.-F., Wang, C.Y., 2013. Distribution of platinum-group elements in magmatic and altered ores in the Jinchuan intrusion, China: an example of selenium remobilization by postmagmatic fluids. Miner Deposita 48, 767–786. https://doi.org/10.1007/s00126-013-0454-7

Qian, G., Brugger, J., Testemale, D., Skinner, W., Pring, A., 2013. Formation of As(II)-pyrite during experimental replacement of magnetite under hydrothermal conditions. Geochimica et Cosmochimica Acta 100, 1–10. https://doi.org/10.1016/j.gca.2012.09.034

Rautenschlein, M., Jenner, G.A., Hertogen, J., Hofmann, A.W., Kerrich, R., Schmincke, H.-U., White, W.M., 1985. Isotopic and trace element composition of volcanic glasses from the Akaki Canyon, Cyprus: implications for the origin of the Troodos ophiolite. Earth Planet. Sci. Lett. 75, 369–383.

Reed, M.H., Palandri, J., 2006. Sulfide Mineral Precipitation from Hydrothermal Fluids. Reviews in Mineralogy and Geochemistry 61, 609–631. https://doi.org/10.2138/rmg.2006.61.11

Regelous, M., Haase, K.M., Freund, S., Keith, M., Weinzierl, C.G., Beier, C., Brandl, P.A., Endres, T., Schmidt, H., 2014. Formation of the Troodos Ophiolite at a triple junction: Evidence from

trace elements in volcanic glass. Chemical Geology 386, 66–79. https://doi.org/10.1016/j.chemgeo.2014.08.006

Reich, M., Kesler, S.E., Utsunomiya, S., Palenik, C.S., Chryssoulis, S.L., Ewing, R.C., 2005. Solubility of gold in arsenian pyrite. Geochim. Cosmochim. Acta 69, 2781–2796.

Reich, M., Chryssoulis, S.L., Deditius, A., Palacios, C., Zúñiga, A., Weldt, M., Alvear, M., 2010. "Invisible" silver and gold in supergene digenite (Cu1.8S). Geochim. Cosmochim. Acta 74, 6157–6173

Reich, M., Deditius, A., Chryssoulis, S., Li, J.-W., Ma, C.-Q., Parada, M.A., Barra, F., Mittermayr, F., 2013. Pyrite as a record of hydrothermal fluid evolution in a porphyry copper system: A SIMS/EMPA trace element study. Geochim. Cosmochim. Acta 104, 42–62.

Revan, M.K., Genç, Y., Maslennikov, V.V., Maslennikova, S.P., Large, R.R., Danyushevsky, L.V., 2014a. Mineralogy and trace-element geochemistry of sulfide minerals in hydrothermal chimneys from the Upper-Cretaceous VMS deposits of the eastern Pontide orogenic belt (NE Turkey). Ore Geology Reviews 63, 129–149. https://doi.org/10.1016/j.oregeorev.2014.05.006

Richardson, C.J., Cann, J.R., Richards, H.G., Cowan, J.G., 1987. Metal-depleted root zones of the Troodos ore-forming hydrothermal systems, Cyprus. Earth Planet. Sci. Lett. 84, 243–253.

Robertson, A., Xenophontos, C., 1993. Development of concepts concerning the Troodos ophiolite and adjacent units in Cyprus. Geological Society, London, Special Publications 76, 85–119. https://doi.org/10.1144/GSL.SP.1993.076.01.05

Robinson, P., Malpas, J., 1990. The Troodos ophiolite of Cyprus: New perspectives on its origin and emplacement, in: OPHIOLITES Oceanic Crustal Analogues, Proceedings of the Symposium "Troodos 1987." The Geological Survey Department, Ministry of Agriculture and Natural Resources, Nicosia, Cyprus.

Rouxel, O., Fouquet, Y., Ludden, J.N., 2004. Subsurface processes at the lucky strike hydrothermal field, Mid-Atlantic ridge: evidence from sulfur, selenium, and iron isotopes 11Associate editor: S. Sheppard. Geochim. Cosmochim. Acta 68, 2295–2311.

Safina, N.P., Melekestseva, I.Y., Nimis, P., Ankusheva, N.N., Yuminov, A.M., Kotlyarov, V.A., Sadykov, S.A., 2016. Barite from the Saf'yanovka VMS deposit (Central Urals) and Semenov-1 and Semenov-3 hydrothermal sulfide fields (Mid-Atlantic Ridge): a comparative analysis of formation conditions. Miner Deposita 51, 491–507. https://doi.org/10.1007/s00126-015-0617-9

Schmidt, K., Koschinsky, A., Garbe-Schönberg, D., de Carvalho, L.M., Seifert, R., 2007. Geochemistry of hydrothermal fluids from the ultramafic-hosted Logatchev hydrothermal field, 15°N on

the Mid-Atlantic Ridge: Temporal and spatial investigation. Chemical Geology 242, 1–21. https://doi.org/10.1016/j.chemgeo.2007.01.023

Schouten, H., Kelemen, P.B., 2002. Melt viscosity, temperature and transport processes, Troodos ophiolite, Cyprus. Earth Planet. Sci. Lett. 201, 337–352.

Seewald, J.S., Seyfried Jr., W.E., 1990. The effect of temperature on metal mobility in subseafloor hydrothermal systems: constraints from basalt alteration experiments. Earth and Planetary Science Letters 101, 388–403. https://doi.org/10.1016/0012-821X(90)90168-W

Seyfried, W., Bischoff, J.L., 1977. Hydrothermal transport of heavy metals by seawater: The role of seawater/basalt ratio. Earth Planet. Sci. Lett. 34, 71–77.

Seyfried, W., Bischoff, J.L., 1977. Hydrothermal transport of heavy metals by seawater: The role of seawater/basalt ratio. Earth and Planetary Science Letters 34, 71–77. https://doi.org/10.1016/0012-821X(77)90107-8

Simon, G., Huang, H., Penner-Hahn, J.E., Kesler, S.E., Kao, L.-S., 1999. Oxidation state of gold and arsenic in gold-bearing arsenian pyrite. American Mineralogist 84, 1071–1079. https://doi.org/10.2138/am-1999-7-809

Tardani, D., Reich, M., Deditius, A. P., Chryssoulis, S., Sánchez-Alfaro, P., Wrage, J., & Roberts, M. P. (2017). Copper–arsenic decoupling in an active geothermal system: A link between pyrite and fluid composition. *Geochim. Cosmochim. Acta*, *204*, 179-204.

Taylor, S.L. (2015). The effect of heap bioleach processes on VMS copper ores, MESci Thesis, Cardiff University, unpub

Thy, P., 1987. Petrogenetic implications of mineral crystallization trends of Troodos cumulates, Cyprus. Geological Magazine 124, 1–11. https://doi.org/10.1017/S0016756800015739

Thy, P., Moores, E.M., 1988. Crustal accretion and tectonic setting of the Troodos ophiolite, Cyprus. Tectonophysics 147, 221–245. https://doi.org/10.1016/0040-1951(88)90188-6 Varga, R.J., Gee, J.S., Bettison-Varga, L., Anderson, R.S., Johnson, C.L., 1999. Early establishment of seafloor hydrothermal systems during structural extension: paleomagnetic evidence from the Troodos ophiolite, Cyprus. Earth Planet. Sci. Lett. 171, 221–235.

Varga, R.J., Moores, E.M., 1990. Intermittent magmatic spreading and tectonic extension in the Troodos Ophiolite: implications for exploration for black smoker-type ore deposits, in: OPHIOLITES Oceanic Crustal Analogues, Proceedings of the Symposium “Troodos 1987.” The Geological Survey Department, Ministry of Agriculture and Natural Resources, Nicosia, Cyprus, pp. 53–64.

Varga, R.J., Moores, E.M., 1985. Spreading structure of the Troodos ophiolite, Cyprus. Geology 13, 846–850.

Vibetti, N.J., 1993. Chemical alteration trends, fluid inclusion patterns and stable isotope compositions in the plutonic sequence of the Troodos ophiolite, Cyprus. Journal of African Earth Sciences (and the Middle East) 17, 193–202. https://doi.org/10.1016/0899-5362(93)90035-O

Von Damm, K.L., 1990. Seafloor Hydrothermal Activity: Black Smoker Chemistry and Chimneys. Annu. Rev. Earth Planet. Sci. 18, 173–204.

Webber, A.P., Roberts, S., Murton, B.J., Hodgkinson, M.R.S., 2015. Geology, sulfide geochemistry and supercritical venting at the Beebe Hydrothermal Vent Field, Cayman Trough. Geochemistry, Geophysics, Geosystems 16, 2661–2678. https://doi.org/10.1002/2015GC005879

White, N.C., Hedenquist, J.W., 1990. Epithermal environments and styles of mineralization: Variations and their causes, and guidelines for exploration. Journal of Geochemical Exploration 36, 445–474. https://doi.org/10.1016/0375-6742(90)90063-G

Williams-Jones, A.E., Heinrich, C.A., 2005. 100th Anniversary Special Paper: Vapor Transport of Metals and the Formation of Magmatic-Hydrothermal Ore Deposits. Economic Geology 100, 1287–1312. https://doi.org/10.2113/gsecongeo.100.7.1287

Wohlgemuth-Ueberwasser, C.C., Viljoen, F., Petersen, S., Vorster, C., 2015. Distribution and solubility limits of trace elements in hydrothermal black smoker sulfides: An in-situ LA-ICP-MS study. Geochimica et Cosmochimica Acta 159, 16–41. https://doi.org/10.1016/j.gca.2015.03.020

Yang, K., Scott, S.D., 2002. Magmatic Degassing of Volatiles and Ore Metals into a Hydrothermal System on the Modern Sea Floor of the Eastern Manus Back-Arc Basin, Western Pacific. Economic Geology 97, 1079–1100. https://doi.org/10.2113/gsecongeo.97.5.1079

Ye, L., Cook, N.J., Ciobanu, C.L., Yuping, L., Qian, Z., Tiegeng, L., Wei, G., Yulong, Y., Danyushevskiy, L., 2011. Trace and minor elements in sphalerite from base metal deposits in South China: A LA-ICPMS study. Ore Geol. Rev. 39, 188–217. https://doi.org/10.1016/j.oregeorev.2011.03.001

Yeats, C. J., Parr, J. M., Binns, R. A., Gemmell, J. B., & Scott, S. D. (2014). The SuSu Knolls hydrothermal field, eastern Manus Basin, Papua New Guinea: an active submarine high-sulfidation copper-gold system. Soc. of Econ Geol.,*109*, 2207-2226.

Brazilian Minerals Group, 2013; Appendix 5B: "HIGH-GRADE COPPER-ZINC SULPHIDE MINERALISATION IDENTIFIED AT MALA PROSPECT – VRECHIA"- accessed 30/07/2018

Figure Captions

Figure 1: Simplified geological map of the 92 Ma Troodos ophiolite. STTFZ = Southern Troodos Transform Fault Zone (after Martin et al., 2018).

Figure 2: Structural domain map of the Troodos ophiolite showing VMS deposits and structural domains based on dyke dip and strike. Simplified from the nine original districts defined by Moores et al. (1990). VMS deposit names analysed in this study are listed from W to E.

Table 1: Summary, location and mineral occurrences in VMS deposits considered in this study. PY = pyrite, CCP= chalcopyrite, SPH= sphalerite, CV= covellite.

Figure 3: Reflected light photomicrographs of common sulfide textures in Troodos VMS. A) Banded pyrite-chalcopyrite in massive ore (Kokkinoyia). B) Late euhedral pyrite overprinting chalcopyrite that is altered to covellite (Phoucasa). C) Colliomorphic pyrite with interstitial chalcopyrite and silica. D) Colloform, crudely layered pyrite (Mala). E) Pyrite overprinted by chalcopyrite with silica and goethite (Kokkinoyia). F) Disseminated euhedral pyrite in chloritised wall-rock with minor interstitial chalcopyrite (Limni). G) Disseminated pyrite infilling vesicles (Kokkinopezula). H) Anhedral aggregates of pyrite lining vein margins from Agrokipia B. I) Photograph of jasper (red) with quartz and feathery pyrite dissolution texture. J) Semi-massive ore from Kokkinoyia, pyrite overprinted by chalcopyrite. K) Close up of euhedral pyrite overprinting chalcopyrite and extensive covellite (Phoucasa). L) Granular upper mound facies, pyrite is rounded and framboidal (Phoucasa). M) Stockwork with massive chalcopyrite and minor subhedral pyrite (Apliki). N) Chalcopyrite, sphalerite and pyrite in quartz from Agrokipia B. O) Subhedral sphalerite occupying the centre of a quartz vein with minor disseminated pyrite (Agrokipia B). Yellow arrows indicate pyrite cores. PY= pyrite, CCP= chalcopyrite, SPH =sphalerite, CV= covellite.

Table 2: Summary of pyrite geochemistry from 20 VMS of Troodos. Maximum (Max), minimum (Min), average, median and standard deviation (σ) (full data and detection limits are available in supplementary material Appendix 1 and 7).

Table 3: Correlation (Linear R values) matrix of trace elements in pyrite (n=1322). Correlation between trace elements is limited with the notable exception of Zn-Cd, Pb-Ag and Au-As.

Table 4: Summary of chalcopyrite geochemistry from 8 VMS of Troodos. Maximum (Max), Minimum (Min), average, median and standard deviation (σ) (full data is available in supplementary material A2).

Table 5: Summary of sphalerite geochemistry from 4 VMS of Troodos. Maximum (Max), Minimum (Min), average, median and standard deviation (σ). *indicates analysis via LA-ICP-MS (full data is available in supplementary material A3).

Figure 4: Average concentration of major and trace elements by mineral in ppm. Ru and Pd are average values of [105,106,108] Pd and [99,101] Ru. Chalcopyrite preferentially incorporates PGE'S, Se, Co and Ni. Pyrite is enriched in Bi, Te, As, Sb and Au. Sphalerite is enriched in Ag and Cd.

Figure 5: LA-ICP-MS Time Resolved Analysis (TRA) of selected sulfide minerals (red arrow indicates laser motion). (A) Pyrite aggregate (Mala) multiple pyrite crystals are identifiable due to variation in TRA shape showing variations from core to rim. (B) Colloform pyrite (Mala) is depleted in solid solution hosted elements (e.g. Se) but enriched in inclusion hosted elements (e.g. Sb). (C) Chalcopyrite (Apliki), note the preferential incorporation of Se in chalcopyrite with a smooth ablation profile. (D) Euhedral pyrite (Apliki) exhibiting a smooth TRA profile for Se and a more jagged profile for Te suggesting variable mechanisms of incorporation in pyrite. (E) Multiple generations of euhedral pyrite demonstrating the variable physicochemical conditions during pyrite precipitation (Apliki). (F) Sphalerite spot analysis (Agrokipia B), note correlation of Cd and Ag with Zn. (G) Euhedral to subhedral pyrite (Skouriotissa); Bi and Te profiles mirror each other possibly suggesting a coupled behaviour.

Figure 6: Concentrations of (A) Au, (B) Ag, (C) Sb, (D) Pb, (E) Te, (F) Se vs. As in pyrite for all Troodos VMS. Red dashed lines define the wedge-shaped zone, points that plot within this zone are hosted in a solid solution and outside as mineral-nanoscale inclusions (after Deditius et al., 2014; Reich et al., 2005, 2010, 2013 and Keith et al., 2016b). Selenium vs. As does not form a wedge shaped zone with high Se concentrations realised at a range of As concentrations- thus supporting Se's incorporation in a solid solution with S. The black dashed line (6A and 6E) represents the solubility limit of Au^0 in pyrite as a function of As (Keith et al., 2018; Reich et al., 2005). Modern SMS data from Keith et al. (2016b).

Figure 7A: Concentration of Te vs. Bi for Skouriotissa (Phoucasa) and Apliki VMS. The moderate positive correlation between Bi and Te suggests Te (R^2= 0.35 and 0.32) may be hosted by Bi-Telluride inclusions or discrete mineral phases (B) Tellurobismuthite (Bi_2Te_3) from Skouriotissa forming along pyrite grain boundaries (Taylor, 2015).

Figure 8: Concentrations of Au vs. As for auriferous VMS deposits of southern Troodos; Kalavasos (n= 39), Mala (n= 6), Mathiatis North (n=107) and the Logatchev hydrothermal field (n=22) (*Keith et al., 2016b). Data shows that at high Au and low As concentrations <1000 ppm Au may be incorporated as Au^0 in mineral- or nanoscale-inclusions in pyrite. A large proportion of points are hosted a as solid solution located within the Au^{+1} zone.

Table 6: Concentration of trace elements between the Solea and Mitsero structural domain (ppm). Solea is enriched in magmatophile elements (Te, Se, Au, Cu) relative to Mitsero.

Figure 9: Selenium/Sulfur ratios in pyrite from VMS of the Solea and Mitsero domains. Dashed line indicates the magmatic-hydrothermal threshold (500) identified by Layton-Matthews et al., (2008). Upper dashed line (1500) shows maximum Se/S for modern MOR SMS (Layton-Matthews et al., 2008). Selenium/Sulfur ratios from Solea are skewed towards magmatic values with a maximum of 9280 whilst Mitsero are lower with a maximum of 640 (also see Appendix A6).

Figure 10: A model of magmatic volatile influx in the Troodos VMS system. Figure (A): Increased magmatic influx into the VMS hydrothermal system at Solea due to increased magmatism and a mobile crack front. Figure (B); influence of lava geochemistry and epidosite formation with Solea epidosite zone containing a higher proportion of mafic (basaltic) Se, Au, Cu rich dykes that are subsequently epidotised releasing relatively higher quantities of Se, Au and Cu into the hydrothermal system. The inverse is true at Mitsero that contains less evolved dykes within the epidosite zone. Figure (C); the effect of a low magmatic influx and a static crack front; brine is not liberated into the hydrothermal system and VMS deposits are depleted in magmatophile elements at Mitsero.

Fig 1

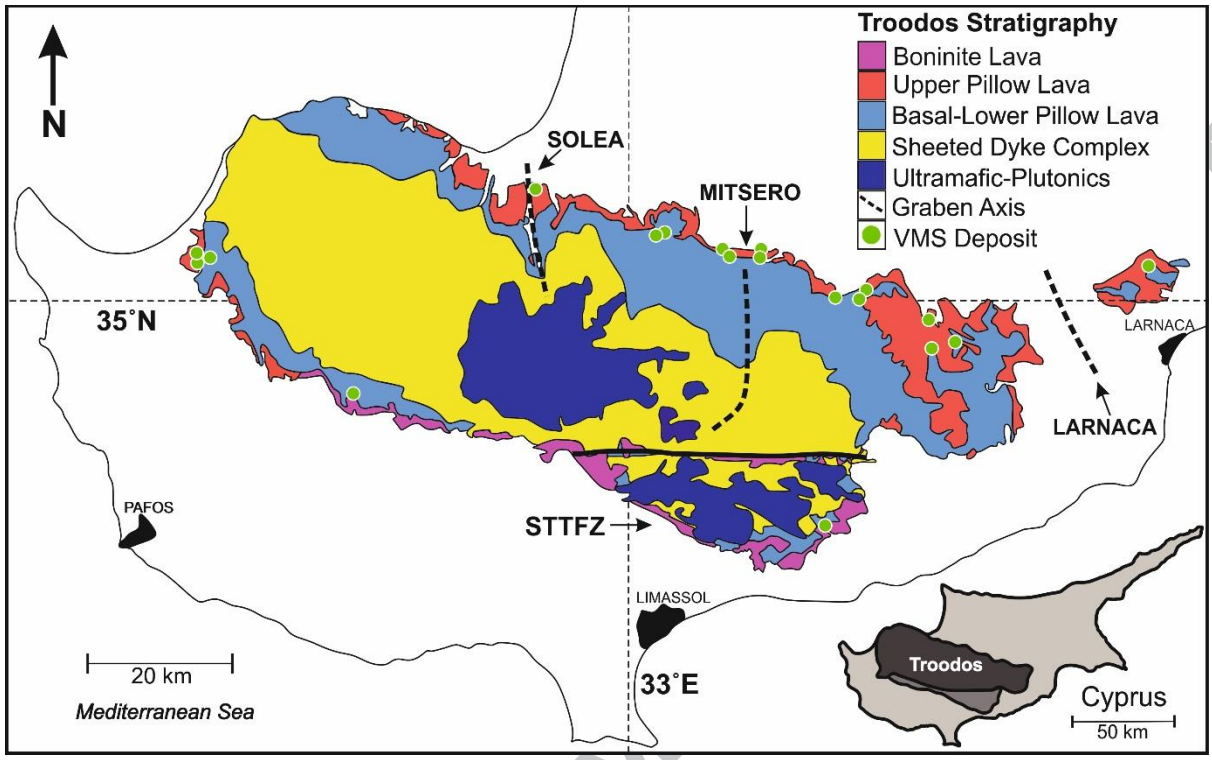

Fig 2

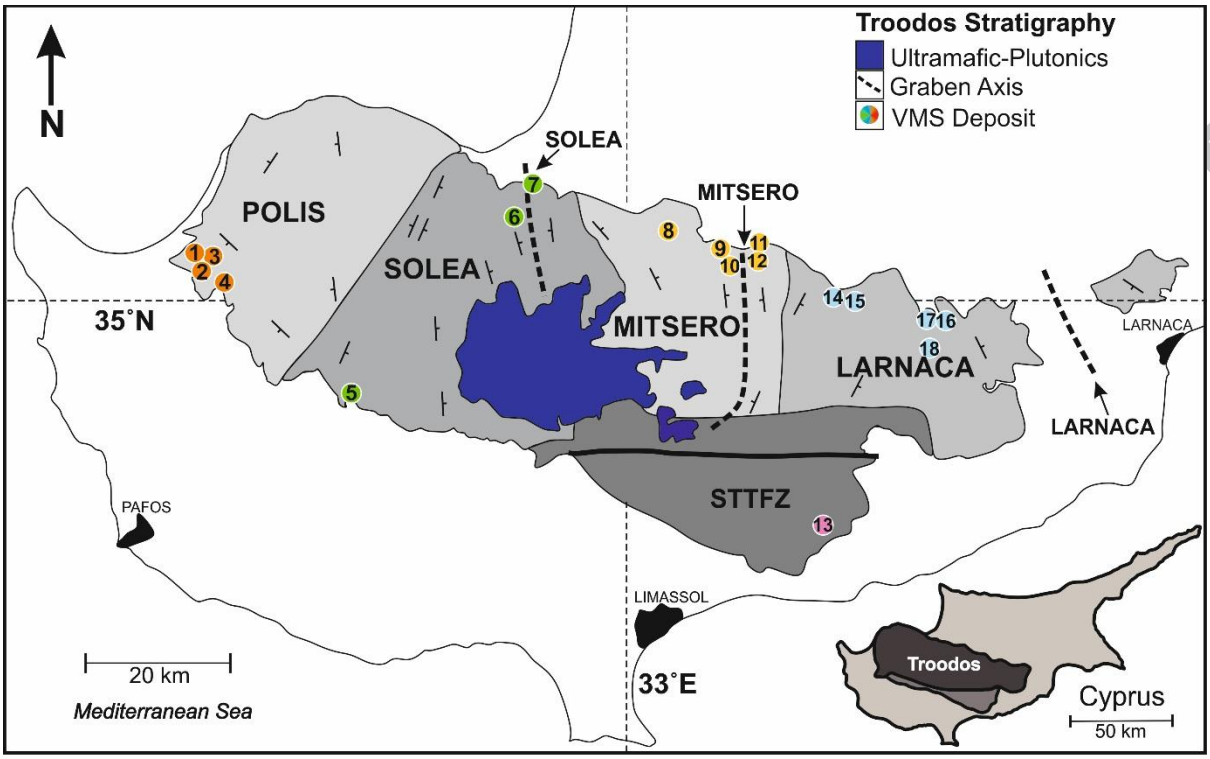

Polis:	Solea:	Mitsero:	STTFZ:	Larnaca:
1. Limni	5. Mala	8. Memi	13. Kalavasos	14. Kambia
2. '77'	6. Apliki	9. Kokkinoyia		15. Kaphedes
3. Kynousa	7. Skouriotissa	10. Kokkinopezula		16. Mathiatis North
4. Pournaji	-Phoenix	11. Agrokipia B		17. Mathiatis South
	- Phoucasa	12. Agrokipia A		18. Sha
	- Three Hills			

Fig 3

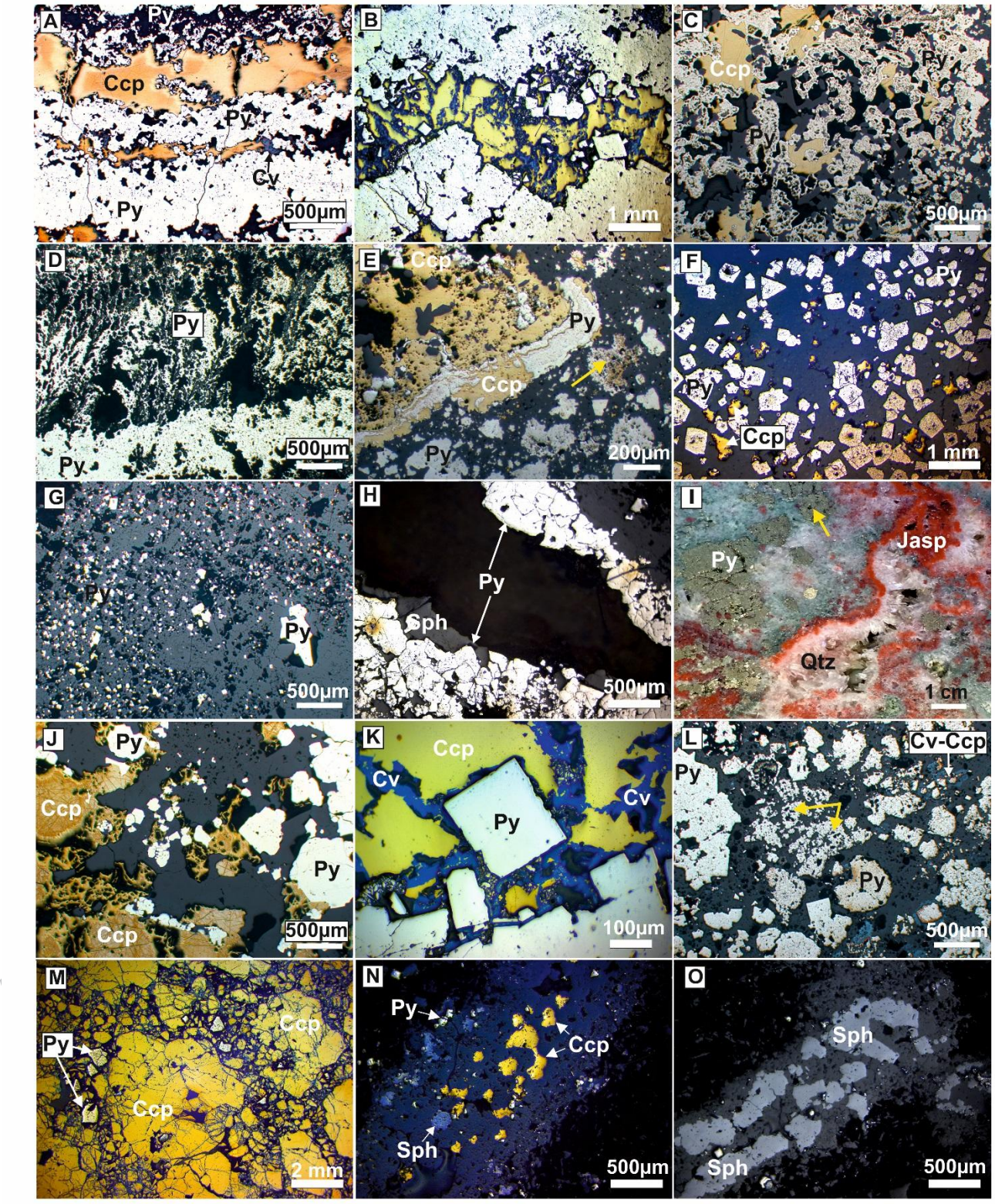
A
Py
Ccp
Py
Cv
Py
500μm
B
1 mm
C
Ccp
Py
Py
500μm
D
Py
Py
500μm
E
Ccp
Py
Ccp
Py
200μm
F
Py
Py
Ccp
1 mm
G
Py
Py
500μm
H
Py
Sph
500μm
I
Jasp
Py
Qtz
1 cm
J
Py
Ccp
Py
Ccp
500μm
K
Ccp
Cv
Cv
Py
100μm
L
Cv-Ccp
Py
Py
500μm
M
Ccp
Py
Ccp
2 mm
N
Py
Ccp
Sph
500μm
O
Sph
Sph
500μm

Fig 4

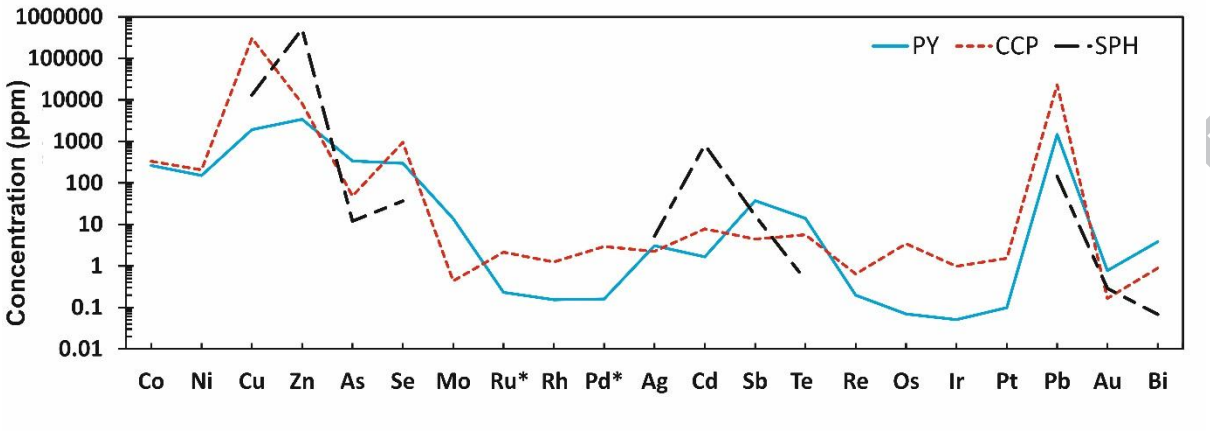

Fig 5

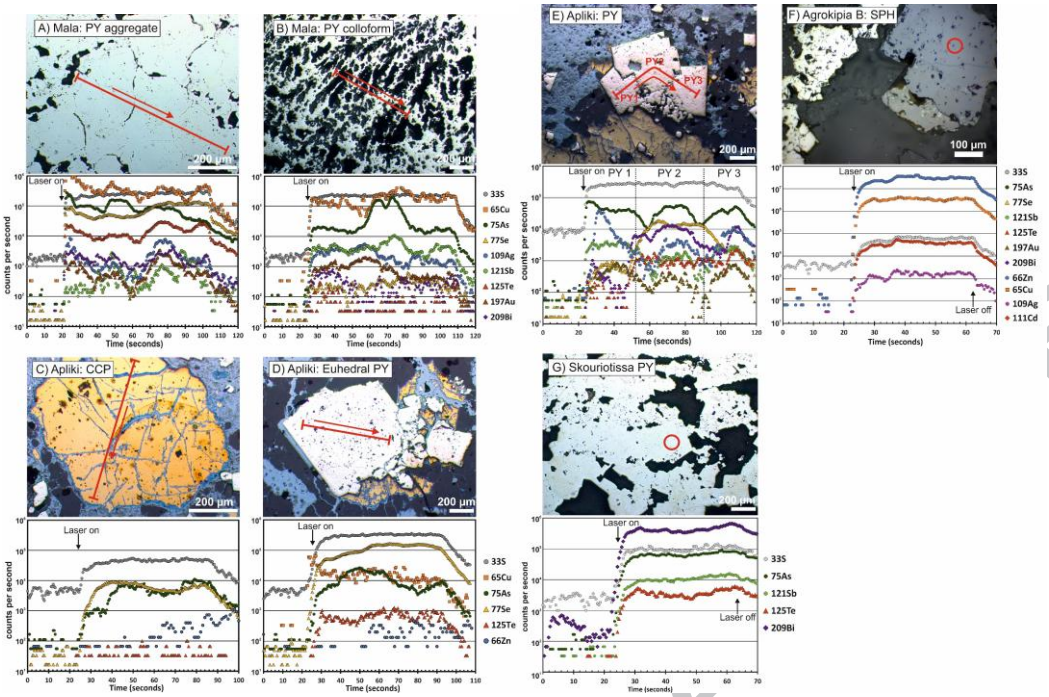

Fig 6

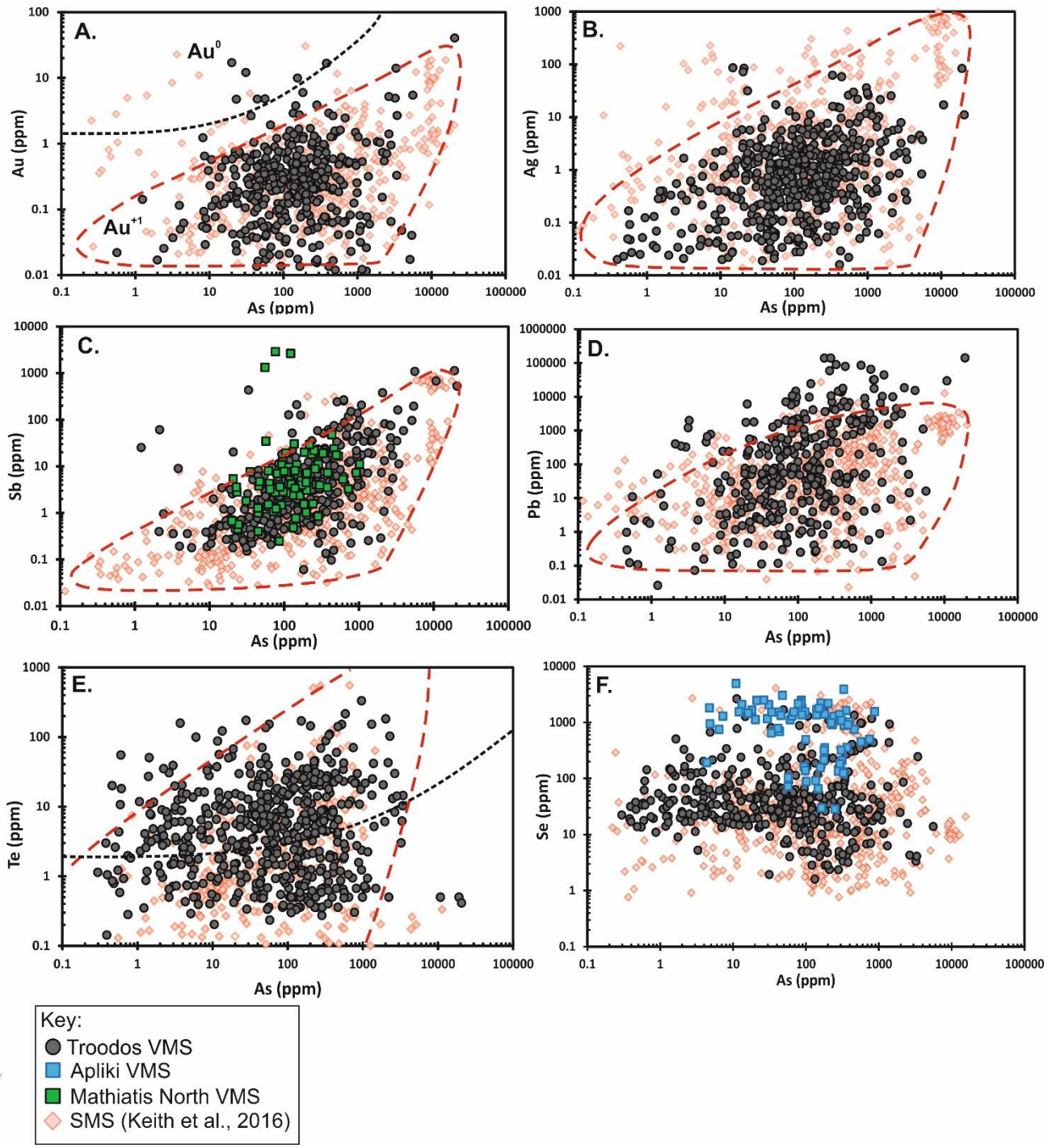

Fig 7

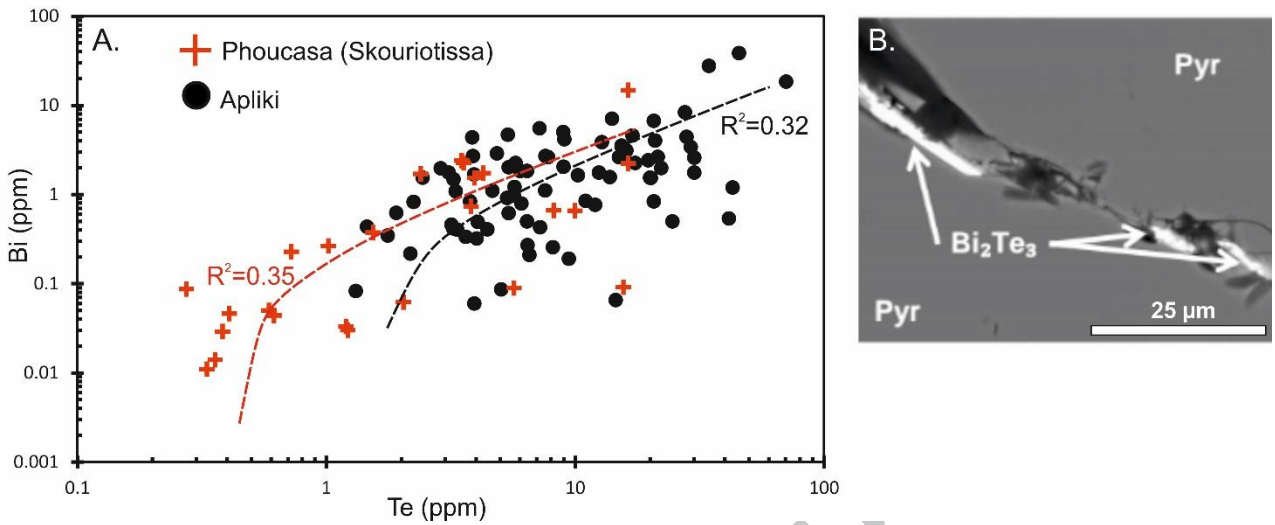

Fig 8

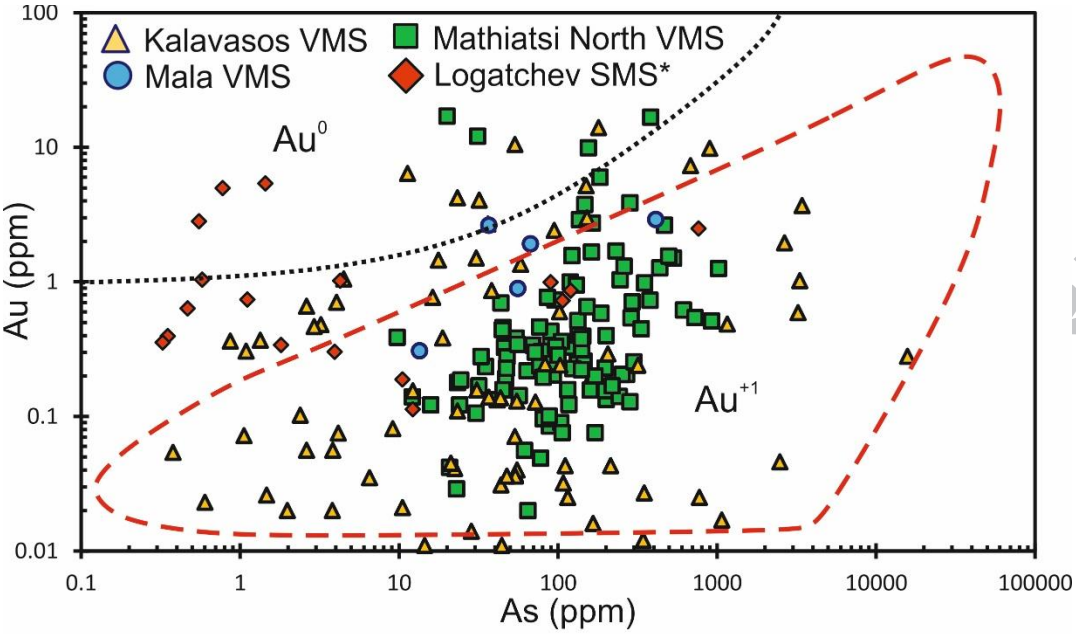

Fig 9

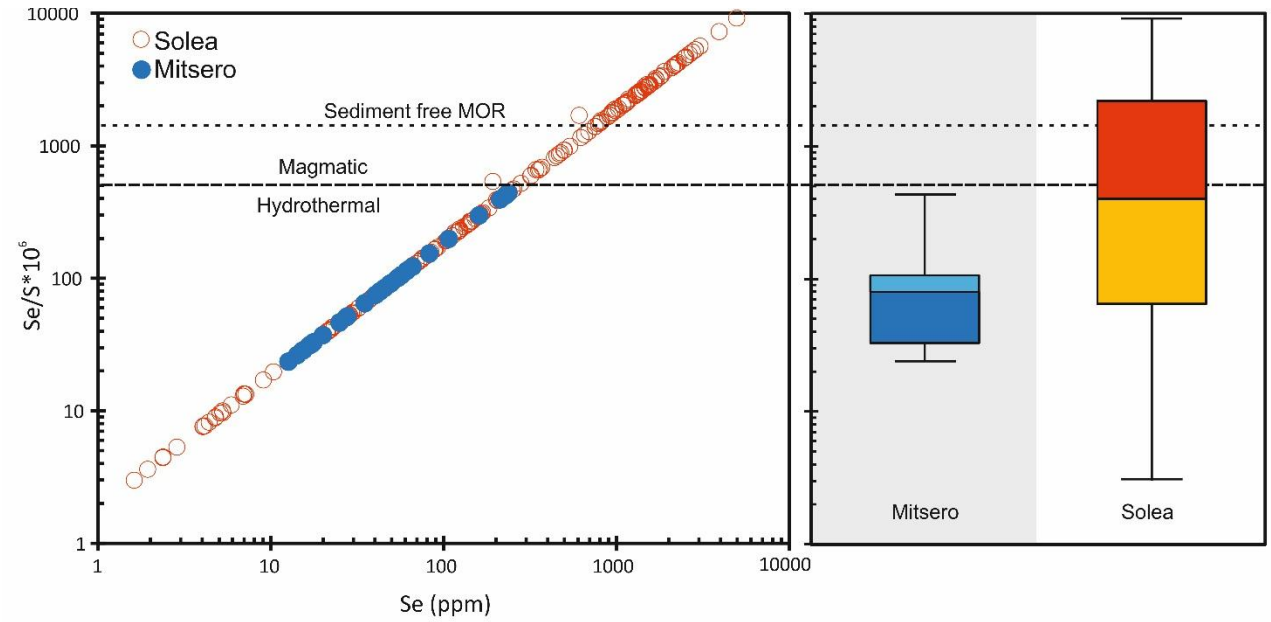

Fig 10

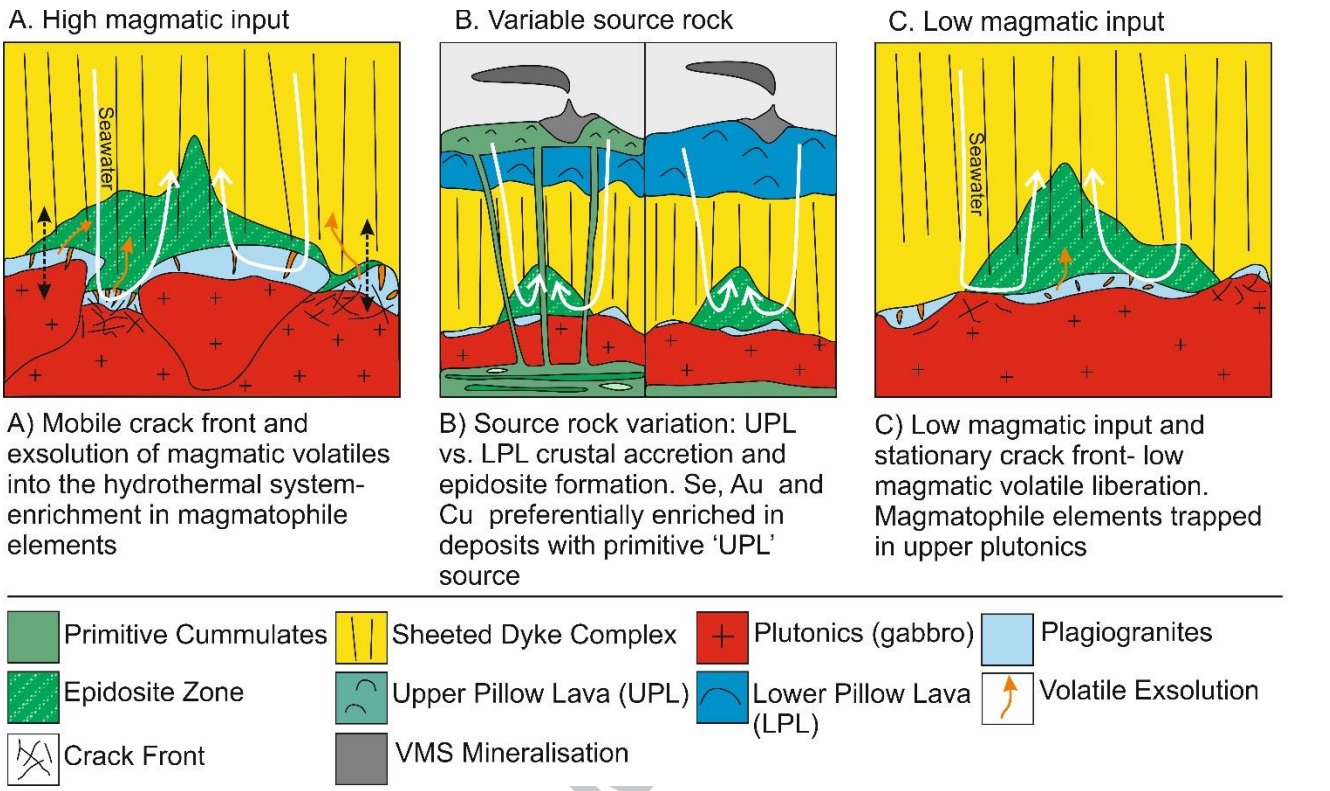

Locality	Location (WGS 1984)	Structural domain	Sample type	Mineral
Limni	045294 3877209	Polis	Disseminated, Massive	PY,CCP
Kynousa/Lysos	045555 3876810	Polis	Massive, Stockwork	PY, SPH, CCP
Pournaji	045529 3876352	Polis	Massive	PY
'77'	045404 3877993	Polis	Massive	PY
Mala	047042 3864323	Solea	Massive	PY
Apliki	048575 3881758	Solea	Stockwork	CV,CCP,PY
Phoucasa	048990 3883713	Solea	Stockwork, Massive	CCP, CV, PY
Phoenix	048993 3884050	Solea	Stockwork, Jasper	CCP, PY
Three Hills	049088 3883189	Solea	Stockwork	CCP, PY
Memi	050366 3877476	Mitsero	Massive, Disseminated	PY
Kokkinopezula	051038 3877259	Mitsero	Jasper	PY
Kokkinoyia	050974 3877946	Mitsero	Stockwork, Massive	PY, CCP
Agrokipia A	051327 3878134	Mitsero	Massive, Disseminated	PY
Agrokipia B	N/A	Mitsero	Stockwork	CCP, PY, SPH
Kaphedes	052394 3871610	Larnaca	Massive, Disseminated	PY
Kampia	052501 3872967	Larnaca	Massive, Jasper	PY
Mathiatis North	053185 3870606	Larnaca	Stockwork, Massive	CCP,PY,SPH
Mathiatis South	053170 3867617	Larnaca	Massive	PY
Sha	053414 3867843	Larnaca	Massive	PY
Kalavasos	052371 3850315	STTFZ	Stockwork	PY

Table 1

Locality		Co	Ni	Cu	Zn	As	Se	Mo	Ag	Cd	Sb	Te	Re	Pb	Au	Bi
Pyrite	***n= 1322***	**ppm**	**ppm**	**%**	**ppm**	**ppm**	**ppm**	**ppm**	**ppm**	**ppm**	**ppm**	**ppm**	**ppm**	**ppm**	**ppm**	**ppm**
Limni	Max	3333	400	0.4	2040	1047	885.6		0.8		6.2	42.9	2.38	5200	0.02	8.99
n = 19	Min	14.1	200	0.01	23.6	20.5	18.8		0.08		0.2	0.7	0.03	226.0	0.02	0.14
	Average	998.9	300	0.14	271.7	278.9	118.0		0.5		1.3	10.2	0.27	1053	0.02	4.0
	Median	551.2	300	0.1	103.5	141.5	44.7		0.5		0.7	5.9	0.07	500		3.3
	σ	972.3	80.0	0.14	543.4	312.7	201.3		0.3		1.7	11.5	0.70	1325		3.2
Kynousa	Max	65.6	11.1	0.13	11560	2168	437	0.4	2.5	18.0	9.3	44.3	0.02	232	0.36	93.3
n = 95	Min	0.07	0.4	<0.01	5.0	0.4	17	0.04	0.03	0.1	0.06	1.1	0.02	0.1	0.02	0.01
	Average	6.4	2.7	0.03	15321	452.7	234.2	0.1	0.5	1.7	2.08	19.6	0.02	34.9	0.15	9.9
	Median	0.9	1.7	0.02	375.8	274.0	240.0	0.08	0.2	0.3	1.1	20.9	0.01	7.0	0.08	1.0
	σ	14.7	1.6	0.03	34864	482.3	132.2	0.1	0.7	3.9	2.9	12.9	0.004	60.3	0.12	22.9
Pournaji	Max	41.2	300	0.02	603.1	341.6	92.0		5.8	6.1	1.1	48.6	0.37	4093		4.4
n = 10	Min	2.1	300	0.02	72.2	19.5	45.3		0.5	1.6	0.3	1.2	0.07	1060		0.2
	Average	12.0	300	0.02	369.9	175.1	63.4		2.6	3.6	0.7	15.9	0.20	2500		1.5
	Median	2.5			476.2	247.7	70.1		1.3	3.4	0.7	21.3	0.07	1700		1.4
	σ	19.5			229.0	148.3	16.4		2.4	1.8	0.4	15.3	0.15	1100		1.4
'77'	Max				136.8	3962	43.6		3.8		58.3	6.1		15385	0.05	3.5
n = 11	Min				21.1	4.3	21.2		0.4		0.3	2.4		1200	0.02	0.2
	Average				66.7	836.7	27.9		2.1		11.4	3.7		7100	0.03	1.1
	Median				42.2	276.2	8.1		2.1		3.7	2.8		5000	0.03	1.0
	σ				61.6	1265	8.1		2.4		21.0	2.0		6300	0.02	1.5

Mala	Max	288.3		1.0	912.2	41	46		6.3	2.8	8.1	14.3	0.12		2.92	1.3
n = 10	Min	10.9		0.07	25.4	2.2	17.0		0.9	2.8	0.2	1.9	0.05		0.31	0.2
	Average	82.4		0.3	309.5	72.5	90.0		4.1	2.8	3.0	6.1	0.09		1.74	0.8
	Median	56.0		0.14	201.0	30.2	50.0		4.8		1.9	4.4	0.09		1.92	0.8
	σ	84.2		0.4	319.8	122.9	133.8		2.2	0	3.3	4.5	0.05		1.12	0.5
Apliki	Max	1892	940.2	1.1	36810	878.1	4942		2.6	4.5	19.6	70.5	5.82	7061	0.95	38.5
n = 98	Min	1.5	186.7	0.01	19.3	4.3	28.5		0.3	4.5	0.4	0.7	0.02	184.5	0.01	0.04
	Average	258.3	459.1	0.2	1396	161.0	1229		0.8	4.5	4.1	11.5	0.59	2097	0.23	2.8
	Median	168.0	400	0.1	64.9	12.7	1157		0.5		2.8	6.5	0.6	1100	0.08	1.5
	σ	303.8	233.7	0.2	5962	158.6	959.7		0.7		4.2	11.8	1.22	2216	0.29	5.4

Locality		**Co**	**Ni**	**Cu**	**Zn**	**As**	**Se**	**Mo**	**Ag**	**Cd**	**Sb**	**Te**	**Re**	**Pb**	**Au**	**Bi**
Pyrite cont.		**ppm**	**ppm**	**%**	**ppm**	**ppm**	**ppm**	**ppm**	**ppm**	**ppm**	**ppm**	**ppm**	**ppm**	**ppm**	**ppm**	**ppm**
Phoucasa	Max	4363	637.8	1.99	2599	399	436.4	37.9	86.4	43.2	6.9	16.4	5.30	8873	4.80	14.8
n = 135	Min	0.04	0.2	<0.01	4.2	3.9	1.6	0.3	0.02	0.2	0.2	0.2	0.01	2.9	0.04	0.01
	Average	193.5	15.7	0.05	258.3	84.3	50.2	13.9	3.2	1.4	1.8	4.2	0.27	185.4	0.57	0.8
	Median	12.8	2.0	0.01	68.7	52.4	10.0	103.0	1.1	0.4	1.3	2.0	0.05	40.0	0.42	<0.01
	σ	564.3	85.6	0.2	487.4	83.5	100.5	10.5	10.4	5.3	1.6	5.1	0.99	1048	0.75	2.3
Phoenix +	Max	5833	7244	12.7	12944	1405	1886	7244	72.5	3.7	51.0	53.0	0.99	6090	0.65	18.2
n = 170	Min	8.4	4.0	<0.01	12.5	0.5	4.0	0.1	0.05	0.3	0.1	0.3	0.02	7.0	0.03	0.01
	Average	510.3	529.8	0.3	627.9	111.8	377.4	297.4	3.30	1.10	4.6	8.3	0.13	175.4	0.22	1.3
	Median	223.7	200.0	<0.01	29.6	33.4	155.0	0.9	0.3	0.8	0.5	5.0	0.07	4.0	0.20	0.5

	σ	847.1	1111	1.5	2525	227.6	487.7	1331	11.6	0.8	14.0	10.2	0.21	872.6	0.17	2.5
Three Hills n=15	Max	1266.9	5426	1.4	12073	564.3	436.4		7.5	27.9	28.2	36.1	0.04	9875	0.48	1.9
	Min	12.4	250.6	0.03	27.0	2.1	17.1		2.9	1.3	15.8	0.5	0.03	204.6	0.02	0.06
	Average	517.0	1522.1	0.5	2384	172.4	114.7		5.2	10.7	21.0	5.8	0.03	3378	0.25	0.8
	Median	401.8	300.0	0.1	35.8	61.7	53.0		5.2	3.0	21.0	1.99	0.03	1700	0.25	0.4
	σ	473.2	2482.8	0.8	4205	267.1	138.0		3.2	14.9	10.2	10.3	0.01	4420	0.33	0.8
Memi n = 11	Max	18.0		0.05	76359	686.0			1.7	30.1	44.3	152.0	0.03		0.09	506.3
	Min	1.2		<0.01	23.1	2.4			0.05	8.9	0.2	0.9	0.03		0.03	0.5
	Average	6.9		0.02	19985	189.0			0.8	17.1	19.3	27.1	0.03		0.06	66.9
	Median	4.3		0.02	204.6	30.4			0.8	12.2	17.4	12.1			0.06	15.6
	σ	7.9		0.02	29899	271.4			0.8	11.4	20.1	48.2			0.03	148.9
Kokkino-pezula n = 10	Max	1713		0.02	36.8	139.9	211.5				0.4	118.1				10.1
	Min	5.5		0.01	17.6	5.1	17.2				0.3	1.1				0.1
	Average	318.0		0.01	26.5	67.7	60.8				0.3	26.2				2.7
	Median	136.4		0.01	27.3	49.4	40.1				0.4	15.7		300.0		1.3
	σ	518.4		<0.01	7.7	58.3	58.6				0.03	36.2				4.2
Kokkinoyia n = 59	Max	223.1		2.1	81011	19082	235.7		84.3	12.5	1123	28.3	0.86	2210	14.11	24.8
	Min	0.8		0.01	11.6	5.6	12.6		0.1	2.3	0.2	0.4	0.02	136.3	0.04	0.1
	Average	31.9		0.1	6270	834.0	77.9		10.6	7.1	56.1	3.3	0.25	709.4	2.08	4.8
	Median	14.4		0.04	173.0	149.0	54.0		3.1	6.2	6.7	3.5	0.03	319.1	0.65	1.7
	σ	45.4		0.3	19384	2879	73.9		19.1	4.5	1790	6.3	0.33	769.6	3.38	6.8

Locality		**Co**	**Ni**	**Cu**	**Zn**	**As**	**Se**	**Mo**	**Ag**	**Cd**	**Sb**	**Te**	**Re**	**Pb**	**Au**	**Bi**

Pyrite cont.		ppm	ppm	%	ppm	ppm	ppm	ppm	ppm	ppm	ppm	ppm	ppm	ppm	ppm	ppm
Agrokipia A	Max	2.6		0.05	5931	1316	61.1		14.9	10.1	55.0	20.5	0.09	14503	0.2	24.6
n = 15	Min	1.2		0.01	11.6	29.5	14.1		0.1	1.2	0.2	0.6	0.02	14503	0.01	0.2
	Average	1.8		0.03	1825	596.3	32.9		3.5	4.6	21.6	5.6	0.06	14503	0.07	7.3
	Median	1.7		0.02	811.1	569.8	28.9		1.6	3.5	21.6	1.7	0.06		0.04	4.7
	σ	0.5		0.01	2002	385.5	18.8		4.6	3.3	18.4	6.7	0.04		0.08	8.8
Agrokipia B	Max	130.9		0.04	251152	5414	82.3		10.3	58.9	195.4	15.4	0.04	10182	0.04	1.8
n= 16	Min	1.4		0.01	15.8	3.5	15.2		0.8	1.2	19.4	0.8	0.03	442.9	0.02	0.1
	Average	30.0		0.02	35771	1816	32.1		4.5	18.4	73.0	3.9	0.03	3811	0.03	0.8
	Median	9.1		0.02	2565	1466 67	20.0		4.0	6.8	63.0	1.3	0.03	3100	0.03	0.6
	σ	40.6		0.01	81957	1876	28.5		3.1	27.1	55.7	6.4	0.01	3478	0.02	0.6
Kaphedes	Max	234.4		0.21	23755	302.2	639.7		0.4	9.8	3.8	21.1	0.04	1360		19.7
n = 12	Min	1.8		0.01	23.0	1.6	31.3		0.3	9.8	0.4	1.5	0.02	191.3		0.06
	Average	54.9		0.07	2516	100.2	242.9		0.4	9.8	1.4	10.2	0.03	574.2		7.5
	Median	3.8		0.03	495.1	59.3	158.2		0.4		0.6	8.9	0.03	400.0		6.5
	σ	84.9		0.08	6719	117.2	238.2		0.03		1.5	6.9	0.01	440.5		6.1
Kambia	Max	561.3		0.04	1974	2840	361.0		7.9		36.5	5.4		18458	0.74	6.0
n = 26	Min	0.8		0.04	15.0	3.8	21.8		0.03		0.2	0.5		223.6	0.01	0.1
	Average	74.0		0.04	326.6	632.4	81.1		1.7		7.1	2.1		4115	0.19	2.4
	Median	20.9			42.1	325.9	35.3		1.2		4.1	1.4		1400	0.06	1.8
	σ	131.8			541.3	840.1	92.8		2.3		9.5	1.4		5655	0.28	2.0
Mathiatis N	Max	1767	410.0	0.46	23282	1021	342.9	159	9.6	8.7	2873	6.6	0.2	140198	17.10	6.6

n = 239	Min	0.06	0.4	<0.01	2.9	5.8	2.9	0.09	0.03	0.2	0.2	0.6	0.02	0.09	0.01	0.01
	Average	94.2	64.0	0.04	59.3	156.4	59.3	21.2	1.3	0.8	72.5	1.6	0.06	2131	1.08	0.6
	Median	4.3	33.0	0.01	17.2	103.0	23.6	5.2	0.8	0.5	4.7	1.1	0.05	330.0	0.31	0.1
	σ	263.2	83.0	0.08	3902	170.3	92.2	32.6	1.5	1.1	396.7	1.4	0.04	14738	2.74	1.3
Mathiatis S n= 21	Max	403.8		0.05	77306	2077	65.3		25.4	5.1	378.3	14.7	0.06	17601	0.13	2.6
	Min	3.3		0.01	16.1	4.0	15.3		0.4	1.6	1.5	5.8	0.06	202.1	0.03	0.08
	Average	49.5		0.03	10868	569.6	38.3		7.6	2.9	123.5	9.9	0.06	3016	0.06	1.4
	Median	9.5		0.03	33.2	568.7	45.9		5.1	3.4	96.9	9.4		2100	0.06	1.5
	σ	104.3		0.01	22667	557.0	21.2		7.7	1.5	126.5	3.5		4261	0.06	1.1

Locality		Co	Ni	Cu	Zn	As	Se	Mo	Ag	Cd	Sb	Te	Re	Pb	Au	Bi
Pyrite cont.		**ppm**	**ppm**	**%**	**ppm**	**ppm**	**ppm**	**ppm**	**ppm**	**ppm**	**ppm**	**ppm**	**ppm**	**ppm**	**ppm**	**ppm**
Shan =90	Max	22.7	53.0	0.3	3201	3391	143	26.2	5.1	9.7	25.2	332		93.1	1.6	20.0
	Min	0.16	0.4	<0.01	16.4	0.5	5.8	0.2	0.05	0.3	0.4	1.1		0.1	0.07	0.02
	Average	5.9	2.7	0.03	93 9.9	512.3	36.8	4.7	0.8	2.4	9.2	70.5		20.6	0.67	4.1
	Median	0.8	2.4	<0.01	407.0	123.0	32.4	1.5	0.4	1.6	6.1	33.0		9.7	0.46	4.1
	σ	8.7	1.9	0.07	1255	882.4	33.1	7.2	1.2	2.3	8.6	77.5		27.1	0.51	5.8
Kalavasos n = 260	Max	3940	159	0.07	5593	20562	777.0	502.0	11.0	1.1	10 82	67.0	0.4	579.0	40.04	14.0
	Min	0.1	0.3	<0.01	2.3	0.3	2.9	0.1	0.02	0.02	0.2	0.1	0.01	0.04	0.02	0.01
	Average	331.6	17.6	0.01	393.3	487.1	60.4	12.5	0.6	0.5	74.2	8.6	0.1	22.9	2.10	1.0
	Median	123.0	7.0	<0.01	32.2	31.4	34.7	1.0	0.1	0.5	5.0	3.8	0.08	1.0	0.12	0.1
	σ	577.5	29.5	0.01	1342	2160	98.6	57.1	1.6	0.2	22 6.1	12.2	0.08	73.2	6.65	2.3

Pyrite	Co	Ni	Cu	Zn	As	Se	Mo	Ag	Cd	Sb	Te	Re	Pb	Au	Bi
Co	1														
Ni	0.22	1													
Cu	0.01	0.02	1												
Zn	-0.05	0.14	-0.01	1											
As	-0.05	-0.03	-0.01	0.03	1										
Se	-0.06	0.21	0.05	-0.09	-0.05	1									
Mo	-0.10	-0.05	-0.02	-0.05	0.33	-0.07	1								
Ag	-0.06	0.03	0.04	0.17	0.30	-0.02	0.05	1							
Cd	-0.05	0.00	0.05	0.73	0.03	-0.03	0.00	0.27	1						
Sb	-0.05	-0.02	-0.01	-0.03	0.30	-0.06	0.23	0.12	-0.02	1					
Te	0.07	0.00	-0.04	0.04	0.02	-0.06	-0.09	-0.10	0.01	-0.06	1				
Re	0.11	0.01	0.00	-0.04	0.02	0.27	-0.18	0.00	-0.07	-0.07	0.19	1			
Pb	-0.06	0.28	0.03	0.17	0.41	-0.05	-0.01	0.52	0.27	0.24	-0.09	0.03	1		
Au	-0.05	-0.03	-0.03	-0.04	0.68	-0.16	0.26	0.09	0.03	0.12	-0.02	-0.05	-0.08	1	
Bi	-0.01	0.00	-0.01	0.30	0.01	0.06	-0.02	-0.02	0.25	-0.02	0.23	0.04	0.06	-0.03	1

Table 3

Locality		Co	Ni	Cu	Zn	As	Se	Mo	Ag	Cd	Sb	Te	Re	Pb	Au	Bi
Chalcopyrite	***n = 150***	**ppm**	**ppm**	**%**	**ppm**	**ppm**		**ppm**	**ppm**	**ppm**	**ppm**	**ppm**	**ppm**	**ppm**	**ppm**	**ppm**
Apliki	Max	29.0	49 3.8	35.8	1831	96.5	3956		3.7	5.9	2.1	30.0	2.9	4800	0.01	12.1
n = 55	Min	1.6	49 3.8	20.8	35.4	17.6	103.7		0.5	1.7	0.4	0.4	0.03	100.0	0.01	0.04
	Average	8.7	49 3.8	31.4	287.5	47.2	1608		2.3	2.8	1.1	4.9	0.7	1100	0.01	0.6
	Median	4.4		31.7	145.7	27.6	1787		2.4	2.0	0.9	2.9	2.9	700.0		0.1
	σ	8.1		2.8	354.5	42.9	1065		1.3	1.8	0.7	6.2	1.3	1300	0.13	2.1
Phoucasa	Max	1335	44 2.4	40.5	5641	51.8	1040		13.1	12.6	5.8	17 1.0	4.7	43000	0.52	9.1
n= 20	Min	1.8	44 2.4	25.8	25.2	2.6	248.8		0.2	1.2	0.3	1.0	0.04	200.0	0.03	0.06
	Average	155.4	44 2.2	30.7	892.7	13.1	593.4		4.7	3.5	2.0	17.8	3.4	14700	0.20	1.5
	Median	15.2		30.0	467.7	4.4	505.1		2.7	2.1	1.1	2.5	0.2	800	0.07	0.4
	σ	338.8		3.3	1551	18.5	231.6		4.5	3.6	2.1	43.8	5.1	1600	0.06	2.5
Phoenix	Max	1.8		35.0	40.1	0.5	923.0	0.2	1.6	3.0		1.6		5400	0.03	0.1
n = 21	Min	0.3		33.8	32.9	0.5	217.0	0.2	0.05	0.7		0.5		900.0	0.04	0.02
	Average	1.0		34.4	36.1	0.5	666.0	0.2	0.8	1.9		0.9		3100	0.03	0.04
	Median	0.9		35.0	40.1		676.0		0.6	2.1		0.8		3000	0.01	0.02
	σ	0.5		0.3	2.5		250.3		0.7	0.9		0.4		2300	1.34	0.02
Three Hills	Max	91.7	95 8.0	29.4	659 271	31 0.3	87.4		16.3	8.9	9.9	4.2	1.6	16000	0.06	0.6
n = 15	Min	26.7	95 8.0	21.2	260.8	4.0	14.7		0.3	1.6	0.9	0.8	0.2	500.0	0.03	0.1
	Average	60.1	95 8.0	25.3	457 81	86.7	36.2		2.4	4.3	3.9	2.0	0.9	4800	0.04	0.3
	Median	61.8		24.5	780.8	16.2	33.2		1.0	4.0	0.9	1.4	0.9	1300	0.03	0.2
	σ	32.6		2.7	169 731	149.5	21.2		4.4	2.2	5.2	1.3	1.0	6600	0.01	0.2
Mala	Max	22.8		32.5	222 480		14.1		4.5	13 4.9		0.7				

n = 3	Min	18.8	31.5	9044		14.1		2.9	4.3		0.7			
	Average	20.2	31.9	85209		14.1		3.9	50.2		0.7			
	Median	19.0	31.6	23804				4.4	11.5					
	σ	2.3	0.6	119195				0.9	73.4					
Kokkinoyia n = 17	Max	179.4	34.7	3226	32	38	3202	6.9	3.0	3.2	27.7	0.1	8124	0.09	13.4
	Min	179.4	16.9	119.7	11	9.5	73.8	0.4	1.1	0.3	0.4	0.04	8124	0.05	0.07
	Average	179.4	29.9	1424	14	13	1437	1.9	2.4	1.3	4.0	0.06	8124	0.07	2.4
	Median		31.4	1375	9.7	18		0.6	2.6	0.9	1.0	0.05		0.07	0.1
	σ		4.3	1142	11	21	1306	2.6	0.6	1.3	7.7	0.03		0.03	5.4

Locality		Co	Ni	Cu	Zn	As	Se	Mo	Ag	Cd	Sb	Te	Re	Pb	Au	Bi
Chalcopyrite	***n = 150***	**ppm**	**ppm**	**%**	**ppm**	**ppm**		**ppm**	**ppm**	**ppm**	**ppm**	**ppm**	**ppm**	**ppm**	**ppm**	**ppm**
Mathiatis N n= 15	Max	4.0		34.9	2457	70.9	79.3	0.7	0.5	3.2	60.7			21700	1.18	0.03
	Min	0.2		33.2	618	1.1	37.4	0.5	0.07	1.0	69.7			2000	0.04	0.02
	Average	1.1		34.6	1754	20.0	54.8	0.6	0.3	2.4	69.7			81900	0.60	0.03
	Median	0.4		34.6	1970	4.0	49.5	0.6	0.4	2.7				5400	0.57	0.03
	σ	1.7		0.4	869.9	33.9	18.3	0.1	0.2	0.8				90000	0.57	<0.01
Kalavasos n = 4	Max	11.2		34.6	5813		8.1		0.1	16.6						
	Min	5.2		33.7	5145		7.5		0.1	10.9						
	Average	8.2		34.1	5479		7.8		0.1	13.8						
	Median	8.2		34.8	5479		7.8		0.1	13.8						
	σ	4.3		0.4	472.4		0.4		<0.01	4.0						

Locality		S	Fe	Zn	Cu	As	Se	Ag	Cd	Sb
Sphalerite	***n= 86***	**%**	**%**	**%**	**%**	**ppm**	**ppm**	**ppm**	**ppm**	**ppm**
		EMPA							**LA-ICP-MS**	
Kynousa	Max	33.28	1.12	65.46	0.19				3400	
n = 2	Min	32.58	0.90	65.22	0.09				3400	
	Average	32.93	1.01	65.34	0.14				3400	
	Median	32.93	1.01	65.34	0.14					
	σ	0.49	0.16	0.17	0.07					
Phoucasa	Max	39.35	29.48	55.97	8.97				2060	
n = 65	Min	33.51	8.64	30.14	0.07				70.0	
	Average	34.72	14.77	47.52	2.21				910.9	
	Median	34.23	13.91	48.42	1.14				720.0	
	σ	1.33	3.79	4.56	2.39				461.0	
Agrokipia B	Max			69.0*	0.62*		20.0	1.3	192.8	1.3
n =10	Min	**Not Analysed**		61.1*	0.46*		20.0	0.7	119.0	0.3
	Average			65.3*	0.53*		20.0	1.1	155.8	0.8
	Median			64.5*	0.52*			1.2	157.7	0.6
	σ			3.0*	0.07*			0.3	26.9	0.4
Mathiati N	Max	33.13	13.98	60.97	0.88	29.7	98.3	26.0	1500	193.0
n = 9	Min	32.10	5.65	52.11	<0.01	1.1	19.5	1.8	400.0	0.2
	Average	32.85	10.59	55.47	0.20	15.4	46.8	8.8	800.0	29.8
	Median	32.89	11.45	54.33	0.14	15.4	37.7	6.2	800.0	0.3
	σ	0.31	2.71	2.89	0.07	20.2	31.6	8.1	353.6	72.2

Table 5

Table 6

Element	Mitsero	Solea
Au	0.3	0.5
Te	5.4	8.6
Se	47	662
Bi	3.2	1.7
Cu	800	1800
Co	116	299
Sb	52	3.2
As	671	119

Graphical abstract

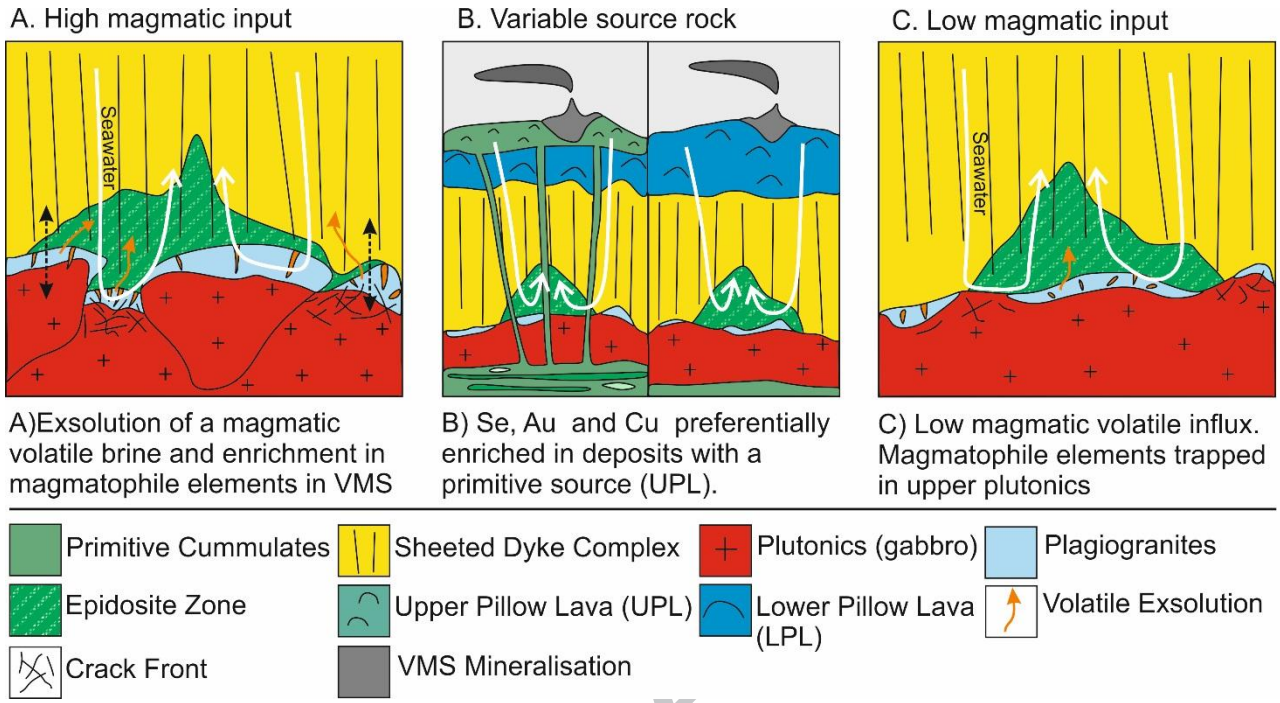

Highlights

- In situ geochemistry of sulfides from 20 VMS deposits spanning the entire Troodos ophiolite, Cyprus
- Partitioning behaviour of trace elements between pyrite, chalcopyrite and sphalerite
- Solubility limits and incorporation of Au, Te, Sb, Pb and Ag in pyrite
- Se/S ratios and trace element profiles as an indicator for variable magmatic volatile influx